Acta Materialia 298 (2025) 121400

Contents lists available at ScienceDirect

Acta Materialia

journal homepage: www.elsevier.com/locate/actamat

Full length article

Role of oxygen in phase stability and mechanical behavior of the bcc HfNbTaTiZr high-entropy alloy during aging

Yujun Zhao [a,*], Maik Rajkowski [a], Yilun Gong [b,c], Stephan Laube [d], Loïc Perrière [e], Alexander Kauffmann [a,d], Jean-Philippe Couzinié [e], Guillaume Laplanche [a], Tong Li [a,*]

[a] Faculty of Mechanical Engineering, Institute for Materials, Ruhr-Universität Bochum, Universitätsstraße 150, 44801 Bochum, Germany
[b] Max Planck Institute for Sustainable Materials, Max-Planck-Straße 1, 40237, Düsseldorf, Germany
[c] Department of Materials, University of Oxford, Parks Road, Oxford OX1 3PH, UK
[d] Institute for Applied Materials (IAM), Karlsruhe Institute of Technology (KIT), Kaiserstraße 12, 76131, Karlsruhe, Germany
[e] Université Paris Est, Institut de Chimie et des Matériaux Paris-Est (UMR7182), CNRS, UPEC, 2-8 rue Henri Dunant, F-94320, Thiais, France

ARTICLE INFO

Keywords:
TiZrNbHfTa
Phase transformation
Atom probe tomography
Transmission electron microscopy (TEM)
mechanical properties

ABSTRACT

The present work aims to explore how oxygen impacts the phase stability and mechanical behavior of the initially single-phase, body-centered cubic (bcc) HfNbTaTiZr high-entropy alloy. For this purpose, transmission electron microscopy and atom probe tomography were employed to investigate the structural and compositional evolutions in two alloys: HfNbTaTiZr and HfNbTaTiZr-3O (3 at.% oxygen) during aging at 500 °C up to 1000 h under an argon atmosphere. Tensile tests and micro-mechanical tests were performed to study the mechanical properties. In the early stage of decomposition of the bcc parent phase in HfNbTaTiZr, Zr-Hf-rich channel-like body-centered tetragonal (bct) features with a thickness of ~2.7 nm form along $<001>_{bcc}$ directions, likely driven by lattice relaxations of the bcc solid solution. Meanwhile, a Zr-Hf-rich hexagonal close-packed (hcp) phase of ~3.6 nm in size forms at the nodes of the bct channels, near which a ~11.1 nm Ti-rich ω phase is present. As aging proceeds, the ω phase dissolves and the bct phase transforms into a distorted hexagonal phase. Similar phases and microstructural features were also observed in HfNbTaTiZr-3O with finer bct channels of ~2.1 nm in width, where the bct-to-hcp transformation is hindered due to the stabilized bct channels by oxygen. After longer aging heat treatments, the ω phase persists accompanied by an increase in oxygen concentration. The microstructures comprised of nanometer-sized bct channels, ω, and hcp phases increase the strength of grain interiors, which can be used to improve the mechanical properties of HfNbTaTiZr in future research.

1. Introduction

Refractory high-entropy alloys (RHEAs) commonly have a body-centered cubic (bcc) crystal structure and are considered promising candidates for application in the aerospace [1,2], nuclear [3,4], and bio-medical industries [5,6]. One of the most prominent RHEAs is the equiatomic HfNbTaTiZr alloy. This alloy exhibits a good combination of strength and ductility under both compressive [7] and tensile [8] loading at ambient temperatures, allowing cold work processing of the alloy [9]. It forms a stable single-phase bcc solid solution at around 1100 °C, whereas secondary phases have been found to form upon aging at intermediate temperatures (500 °C – 900 °C) [10–14]. For example, Chen et al. [11] investigated the phase stability of a coarse-grained HfNbTaTiZr alloy with a mean size of ~50 μm between 550 °C and 1000 °C. They observed two distinct bcc phases at 900 °C, i.e. the bcc matrix (bcc1) and another Nb-Ta-rich bcc2, while at 700 °C, their transmission electron microscopy (TEM) and atom probe tomography (APT) investigations revealed three phases, i.e., the bcc matrix decomposes into a Nb-Ta-rich bcc2 phase, with the same crystallographic orientation as the matrix, and a Zr-Hf-rich hexagonal close-packed (hcp1) phase exhibiting the Burgers orientation relationship (BOR) with the bcc phases. At 550 °C, the volume fraction of the original bcc matrix further decreased. These observed phase constitutions have been qualitatively reflected in the work of Schuh et al. [10]. The authors studied the stability of a nanocrystalline HfNbTaTiZr fabricated by high-pressure torsion with a mean size of ~50 nm, whose phase decomposition was accelerated due to the high density of defects acting as nucleation sites and fast diffusion pathways. The bcc solid solution

* Corresponding authors.
E-mail addresses: yujun.zhao@rub.de (Y. Zhao), tong.li@rub.de (T. Li).

https://doi.org/10.1016/j.actamat.2025.121400
Received 13 March 2025; Received in revised form 19 July 2025; Accepted 3 August 2025
Available online 5 August 2025
1359-6454/© 2025 The Authors. Published by Elsevier Inc. on behalf of Acta Materialia Inc. This is an open access article under the CC BY license (http://creativecommons.org/licenses/by/4.0/).

decomposed into bcc1 and bcc2 phases at 900 °C, whereas three phases, namely Zr-Hf-rich bcc1, Nb-Ta-rich bcc2, and Zr-Hf-rich hcp1 phase, were identified at 800 °C.

At temperatures ≤ 500 °C, the phase stability of the HfNbTaTiZr alloy remains controversial. Schuh et al. [10] reported that the alloy aged at 500 °C for 100 h is composed of bcc2 and hcp1 phases, while Moschetti et al. [14] observed an additional hcp2 phase under the same aging condition in the HfNbTaTiZr alloy with an average grain size of ~40 nm. However, the composition and formation mechanism of the hcp2 phase were not addressed. Notably, a microhardness evolution of the alloy aged at 500 °C for different durations was observed in these two works [10,14], which exhibits a maximum hardness value after ~1 h of aging and subsequent softening as the aging time increased. The hardening was thought to be related to high defect mobility and the retained solid solution strengthening after a short aging time at 500 °C [10]. The gradual growth of the grains, decreased defect density, and reduced solid solution strengthening during aging were proposed to account for the softening after 100 h [14]. Nevertheless, direct evidence linking microstructural evolutions and mechanical behaviors was missing.

In addition to these bcc and hcp phases, which are considered stable in the HfNbTaTiZr alloy, metastable phases and local chemical clusters have also been reported, typically at temperatures ≤ 500 °C. Yasuda et al. [13] found the presence of spherical ω phase with a size of ~10 nm after aging at 400 °C for 24 h, while Wang et al. [15] observed the deformation-induced ω phase with a lath-like morphology during tensile testing at 227 K and 77 K. ω phase is a well-known metastable phase that forms in Ti-, Zr-, and Hf-alloys and can serve as a nucleation site for hcp-phase precipitation. Compared to the extensive study of the ω phase in traditional alloys, the formation mechanism of this phase in the HfNbTaTiZr alloy lacks thorough investigation. Wu et al. [16] observed Zr-rich clusters along $<001>_{bcc}$ directions, promoted by H interstitials in the bcc lattice, whereas similar microstructural features were found in the alloy aged at 1800 °C in the work of Maiti and Steurer [17], who did not report the effects of interstitial elements. This raised the question of the temperature-dependent stability of such chemical clusters and the role of interstitials.

Indeed, interstitial elements have been found to influence the phase stability and properties of RHEAs. Doping 2 at.% N into the $Ta_{0.5}Nb_{0.5}HfZrTi$ alloy led to the formation of chemical short-range clusters in bcc single phase, which was claimed to increase the strength and ductility of the alloy simultaneously. The stress-induced position changes of N between the chemical clusters and random matrix was proposed to be the reason for high damping capacity of the alloy [18]. Such chemical short-range clusters were also reported in the TiZrHfNb and $Ta_{0.5}Nb_{0.5}HfZrTi$ alloys with 2 at.% O addition, exhibiting superior mechanical ductility than the alloys doped with N [18,19]. For the HfNbTaTiZr HEA, O could strongly affect its phase stability due to the high affinity for O of the alloying elements, especially Ti, Zr, and Hf [20–23]. Furthermore, density functional theory calculations suggested an attraction between non-compact screw dislocation cores and interstitial atoms (such as O, N and C), explaining observed dynamic strain hardening behaviors at high temperatures [24]. Recently, by performing long-term heat treatments up to 1000 h, Poulain et al. [25] showed that HfNbTaTiZr is single-phase bcc at 900 °C, but the addition of O induced decompose of the bcc phase into bcc2 and hcp1 phases. O is known to stabilize the isothermal ω phase and increases the formation energy barrier of the athermal ω phase in Ti-alloys [26–28]. However, the influence of O on the formation mechanism of ω phase and its relationship with the hcp phase in HfNbTaTiZr has not received much attention. Also, the effects of O on the stability of the local chemical clusters observed in the previous works [16,17] during long-term heat treatment is poorly understood.

In short, compared to the already established phase stability of the HfNbTaTiZr at high temperatures, its stability at temperatures ≤ 500 °C needs to be further elucidated, particularly regarding the impact of O. This is essential for broadening the application temperature range of the alloy. To address this, the current work focuses on the aging behavior of the alloy at 500 °C to ensure measurable kinetics. The first objective of this study is to clarify the role of O in the phase stability of the initially single-phase bcc HfNbTaTiZr alloy at 500 °C. Two alloys with nominal atomic compositions $Hf_{20}Nb_{20}Ta_{20}Ti_{20}Zr_{20}$ (HfNbTaTiZr) and $Hf_{19.4}Nb_{19.4}Ta_{19.4}Ti_{19.4}Zr_{19.4}O_{3.0}$ (HfNbTaTiZr-3O) were produced and aged at 500 °C from 1 h to 1000 h followed by TEM and APT to investigate structural and compositional evolutions. This will provide a deeper understanding of the formation and the stabilization of the nanosized ω phase/chemical clusters/hcp phase [11,13,15,17] and potentially enable microstructural design via metastable phases for improved mechanical properties in future work. The second objective of the present work is to study how O and the formation of secondary phases affect mechanical properties, which were investigated at different scales using tensile, microhardness, and micropillar compression tests.

2. Materials and methods

The HfNbTaTiZr was synthesized by arc melting from high-purity elements (purity > 99.95 wt.%) under an Ar atmosphere. A fully recrystallized microstructure was obtained by cold rolling with a total thickness reduction of ~80 % (around 30 passes in total), and subsequent homogenization in a He atmosphere at 1100 °C for 5 h. The alloy was confirmed to be a homogeneous single-phase bcc solid solution with a mean size of ~80 μm [29,30]. The HfNbTaTiZr-3O was also arc melted from high-purity elements (purity > 99.95 wt. %) with the addition of TiO_2 in an AM/0.5 furnace under an Ar atmosphere, supplied by Edmund Bühler GmbH (Germany). The as-cast alloy was encapsulated in an evacuated fused silica ampoule and homogenized at 1200 °C for 48 h. A single-phase bcc solid solution with an average size of ~50 μm with randomly distributed elements was obtained after the homogenization [30]. For both alloys, the samples in the homogenized state are hereafter referred to as the as-received condition. It is noteworthy that the material processing methods are different for the two alloys because they differ in mechanical behavior and phase stability. Despite the different processing routes of the two alloys, their as-received states have similar initial microstructures, as discussed in supplementary material section D and F. Cuboidal samples of approximately $5 \times 5 \times 2$ mm^3 were cut from the as-received HfNbTaTiZr, whereas wedge-shaped samples (~60° sector) with a radius of ~5 mm and a thickness of ~5 mm were prepared from the as-received HfNbTaTiZr-3O. These samples were encapsulated in glass tubes in an Ar atmosphere, and aged at 500 °C for 1 h, 10 h, 100 h, and 1000 h, followed by water-quenching.

Microstructural characterizations were carried out with a JEOL JSM-7200F scanning electron microscope (SEM) equipped with an electron backscatter diffraction (EBSD) detector. X-ray diffraction (XRD) measurements were performed on a Bruker D8 Discover with an Incoatec High Brilliance Iμs Cu Kα X-ray source (0.154184 nm) and a Vantec-500 2D-detector in Bragg-Brentano geometry allowing the collection of X-rays in a 2θ-range of ~40° in a single frame. Four frames were taken stepwise from $2\theta = 10°$ to $2\theta = 90°$ with an increment of $2\theta = 20°$

TEM lamellae and APT specimens were prepared by site-specific lift-out and polishing procedures using an FEI Helios G4 CX dual-beam focus ion beam (FIB) [31,32]. TEM examination was performed on a Tecnai G2 F20. APT experiments were carried out with a LEAP 5000XR operated at 60 K with a target evaporation rate of 5 ions per 1000 pulses, and a pulse frequency of 125 kHz. Data acquisition was performed in voltage-pulsing mode with a pulse fraction of 20 % for the following samples: as-received HfNbTaTiZr, 1 h-HfNbTaTiZr, as-received HfNbTaTiZr-3O, 1 h-HfNbTaTiZr-3O, 10 h-HfNbTaTiZr-3O and 100 h-HfNbTaTiZr-3O. The laser-pulsing mode was applied with a laser energy of 50 pJ for the samples: 10 h-HfNbTaTiZr, 100 h-HfNbTaTiZr, 1000 h-HfNbTaTiZr, and 1000 h-HfNbTaTiZr-3O. Since Hf can be evaporated together with H atoms, which stem from the residual H_2 gas

in the APT analysis chamber [33] or are implanted during sample preparation by FIB [34], the evaporated HfH^{2+} molecular ions have very close mass-to-charge ratio to Ta^{2+}ions in laser-pulsing mode. This peak overlap causes inaccuracy of Hf and Ta concentration in laser-pulsing mode (~±4 at.%), which is a systematic error. However, the evaporation field of one phase does not change significantly when a constant laser energy and base temperature are applied [35]. Hence, the compositional evolution of the alloy is not strongly influenced by our experimental setup. Three-dimensional (3D) APT data were reconstructed and analyzed using the AP Suite 6 software.

To study the role of O and secondary phases on mechanical properties, tensile tests with a strain rate of 10^{-3}/s were performed on HfNbTaTiZr and HfNbTaTiZr-3O in the as-received condition and on HfNbTaTiZr aged for 10 h. Tensile specimens were machined with a (0.8 × 4)-mm^2 cross-section and 20-mm gauge length. Two tests were performed for each condition to investigate reproducibility. The influence of microstructural evolution on hardening mechanisms was studied by microhardness experiments performed in a Carat 930 hardness tester with a force of 0.05 kg maintained for 10 s. To ensure statistical relevance, 15 indents were conducted for each condition and each indent was performed in a different grain to average the hardness over multiple crystallographic orientations. Micropillar compression tests were conducted in $<001>_{bcc}$-oriented grains of the alloys aged under different conditions. For this purpose, the MTEX toolbox [36] in MATLAB was used to identify suitable grains with a maximum deviation of 5° from $<001>_{bcc}$. At least six micropillars with a diameter of 2.5 μm and height of 6.25 μm were FIB-milled and tested at a constant displacement rate of 50 nm/s. These tests were performed in-situ in an FEI Quanta 650 ESEM equipped with an ASMEC UNAT-SEM nanomechanical testing system and a 10-μm diameter diamond flat punch indenter tip.

3. Results

3.1. Phase stability of HfNbTaTiZr during aging at 500 °C

The microstructures of HfNbTaTiZr after different heat treatments were investigated by backscatter electron (BSE) imaging in the SEM (Fig. S1). No microscale secondary phases were observed in the as-received state and after aging at 500 °C for 1 h, while fine microstructures within grains were detected after longer aging durations (between 10 and 1000 h). Selected area electron diffraction patterns (SADPs) were recorded by TEM within grains of the bcc matrix to further investigate possible microstructural changes at the nanoscale. Fig. S2 confirms that the as-received and 1-h aged HfNbTaTiZr is indeed single-phase solid solution with a bcc structure.

As the aging time increases to 10 h, the bcc diffraction spots of HfNbTaTiZr show diffuse streaks along $<001>_{bcc}$ directions, see blue arrows in Fig. 1a. Meanwhile, additional diffraction spots are observed in Fig. 1a (e.g., one spot is marked with a light blue circle), corresponding to an hcp crystal structure observed along $a < 11\bar{2}0>_{hcp}$ zone axis (ZA). Figs. 1b and 1c are the dark-field (DF) micrographs taken by selecting the regions marked with white (containing both diffuse streaks and hcp spots) and blue (including only one hcp variant) circles, respectively, in Fig. 1a. In Figs. 1b and c, the alloy exhibits a network-like microstructure consisting of perpendicular channels with a mean thickness[1] of (2.7 ± 0.9) nm and separating cuboids with an average edge length of (20.0 ± 7.2) nm, with hcp particles (mean size: (3.6 ± 1.6) nm) mainly located at the nodes of the channels. After tilting to $<011>_{bcc}$ ZA (Fig. 1d), ω spots are detected at 1/3 and 2/3 of the distance between $\{21\bar{1}\}_{bcc}$ reflections, while hcp spots are observed in between. The three phases have the classic BOR $\{110\}_{bcc} || \{0001\}_{hcp} || \{11\bar{2}0\}_{\omega}$ and $<1\bar{1}1>_{bcc} || <11\bar{2}0>_{hcp} || <0001>_{\omega}$ [37,38]. The DF TEM images in Figs. 1e and 1f, recorded from the green and blue circles in Fig. 1d, show ω with a mean size of (11.1 ± 1.0) nm and hcp particles, respectively, without any specific spatial correlation between them.

After aging for 100 h (Fig. 1*g*), the two variants of hcp phase remain, as indicated by the presence of distinct diffraction spots, but the diffuse streaks near the bcc spots have weakened and a discontinuous diffraction ring separated from the bcc spots has emerged. The interplanar distance of ~0.28 nm corresponding to this diffraction ring is the same as that between $\{10\bar{1}0\}_{hcp}$ planes, whose formation is confirmed by XRD measurements (see Fig. S7). The DF micrograph in Fig. 1h, taken from the white circle in Fig. 1*g*, shows that the channels have significantly grown, reaching a mean thickness of (22.2 ± 8.9) nm, compared to the 10-h aged channels with only (2.7 ± 0.9) nm observed with the same $<001>_{bcc}$ ZA. Meanwhile, the inter-channel distance has increased from (20.0 ± 7.2) nm to (64.4 ± 16.1)nm with increasing aging time from 10 h to 100 h, indicating that some of the channels have dissolved. Similar to the 10-h aged condition, the hcp particles along $<11\bar{2}0>_{hcp}$ ZA with a mean size of (28.0 ± 6.8) nm are located at the channel nodes after 100 h of aging, Fig. 1i. The number density of hcp phase at the nodes decreases significantly from 1215 to 193 μm^{-2} as the aging time increases from 10 to 100 h.

Finally, the microstructure has further coarsened after aging for 1000 h, i.e., the average channel thickness increased to (33.6 ± 20.1) nm (Fig. 1k, $<001>_{bcc}$ ZA). The number density of large hcp particles (mean size: (37.3 ± 11.3) nm, Fig. 1l) at the nodes further decreases to 151 μm^{-2}, while the ω phase had already vanished after aging for 100 h.

The diffuse streaks observed in Fig. 1a after aging for 10 h might arise from nanoscale structural changes. To understand their origin, high-resolution transmission electron microscopy (HRTEM) images were acquired along different ZAs of the 10-h aged HfNbTaTiZr. Like in Fig. 1b, perpendicular channels aligned along $<001>_{bcc}$ directions, dividing the bcc matrix into cuboidal regions, are observed in Fig. 2a. From this HRTEM image, two Fast Fourier Transform (FFT) images were obtained from the regions marked with dark (channel) and light blue (channel node) frames, which are shown in Figs. 2b and 2c, respectively. The FFT image of the channel in Fig. 2b corresponds to a body-centered tetragonal (bct) structure. This structure is determined by tilting the same TEM sample to $[001]_{bcc}$ (Fig. 2a) and $[011]_{bcc}$ (Fig. 2d) ZAs and fitting the observed diffraction spots of the channels with simulated diffraction patterns. The spots of the channels marked in blue in Figs. 2b and 2e match a bct phase with a = (0.34 ± 0.01) nm, c = (0.48 ± 0.01) nm along $[100]_{bct}$ ZA and $[110]_{bct}$ ZAs, respectively. The tilt angle between the $[001]_{bcc}$ and $[011]_{bcc}$ ZAs was measured to be 45°, exactly the angle between $[100]_{bct}$ and $[110]_{bct}$ ZAs. Also, the simulated SADPs of the bct structure in Fig. S3 show a good agreement with the experimental observations, suggesting the bct structure of the channels. The unit cells of bcc (marked in orange) and bct (marked in blue) shown in Fig. 2b exhibit the tetragonal distortion of the original bcc structure after 10 h of aging. As indicated by Figs. 2b and 2e, the bcc matrix has an orientation relationship to the bct channels with three inequivalent variants, namely $[010]_{bct} || [001]_{bcc}$ and $(00\bar{1})_{bct} || (100)_{bcc}$, $[100]_{bct} || [001]_{bcc}$ and $(0\bar{1}0)_{bct} || (100)_{bcc}$, and $[001]_{bct} || [001]_{bcc}$ and $(100)_{bct} || (100)_{bcc}$, see Fig. S4). At the channel node, hcp spots are observed along $<11\bar{2}0>_{hcp}$ ZA (Fig. 2c), consistent with the DF image in Fig. 1c. The BOR among bcc, hcp, and ω phase are revealed in Fig. 2f, which is in line with the SADP in Fig. 1d

The nanoscale structures of coarse channels and hcp particles at nodes after aging for 100 and 1000 h are displayed in Figs. 2*g* and 2j, respectively. The spots in the FFT images (Figs. 2h and 2k) from the channels (obtained from the framed regions numbered 1 in Figs. 2*g* and 2j, respectively) do not perfectly match an hcp structure, whereas the spots at channel nodes (see framed regions numbered 2 in Figs. 2*g* and 2j) clearly do, as revealed by the FFT images in Figs. 2i and 2l Indeed,

[1] The error ranges correspond to the standard deviations of the dimensions measured from TEM micrographs. This applies to all TEM-based size investigations in what follows.

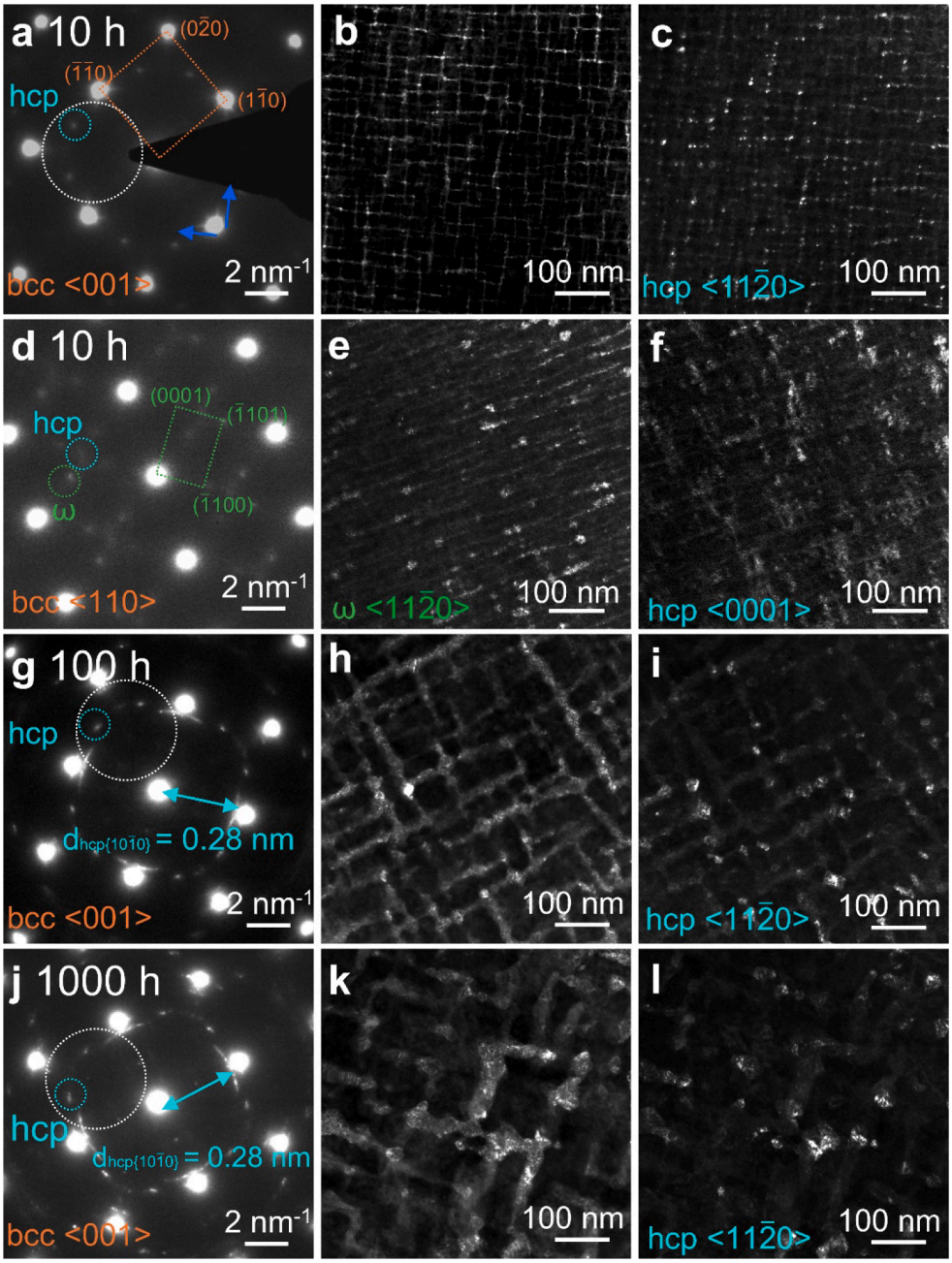

Fig. 1. Microstructural evolution in the initially single-phase, bcc HfNbTaTiZr HEA during aging at 500 °C for (a-f) 10 h, (g-i) 100 h, and (j-l) 1000 h, revealing the formation of an hcp phase (highlighted in light blue) in all cases and an ω phase (green) only in the 10-h aged alloy. SADPs obtained along the (a, g, j) $<001>_{bcc}$ and (d) $<011>_{bcc}$ ZAs are shown in the first column. From the white (or green) and blue circles highlighted in the first column, DF TEM images were obtained, which are displayed in the second and third columns of the corresponding states, respectively. Note that only one diffraction spot was selected to record the SADPs taken from the green and blue circles, while several diffraction spots are included within the white circles.

while the interplanar distances marked in Figs. 2h and 2k are ~0.28 nm, which is close to the expected value for prismatic {10$\bar{1}$0} planes of an ideal hcp phase. The angles between these planes are 69° and 74°, which differ from 60° for an ideal hcp structure, suggesting the phase transformation from bct to ideal hcp phase has not been completed. The observed phase within the channels might exhibit intermediate crystal structures in the pathway of bcc-to-hcp transition. Such an intermediate phase is regarded as a distorted hcp with the rotation of prismatic planes, which could be an orthorhombic structure with space group Cmcm (see Fig. S5). These observations were complemented by XRD analyses, which show the presence of bcc and hcp phases after aging for 100 h and 1000 h (Fig. S7), indicating that the intermediate phase exhibit similarities to the equilibrium hcp phase regarding crystallographic symmetry, which results in the XRD peak overlaps of the two phases [39,40]. The phase transformation sequence from bcc to hcp through orthorhombic usually enables the BOR [41]. Additionally, the transition sequence from high symmetry bcc structure through bct to orthorhombic with gradually reduced symmetry has been proposed in [42]. Similar phase transition pathway could occur in HfNbTaTiZr, i.e. bcc → bct → orthorhombic → hcp. However, the determination of the nanoscale distortion requires further investigations in future.

In summary, based on our experimental results, we conclude that the ideal hcp structure is likely the equilibrium phase, whose formation has not been completed even after aging at 500 °C for 1000 h in HfNbTaTiZr.

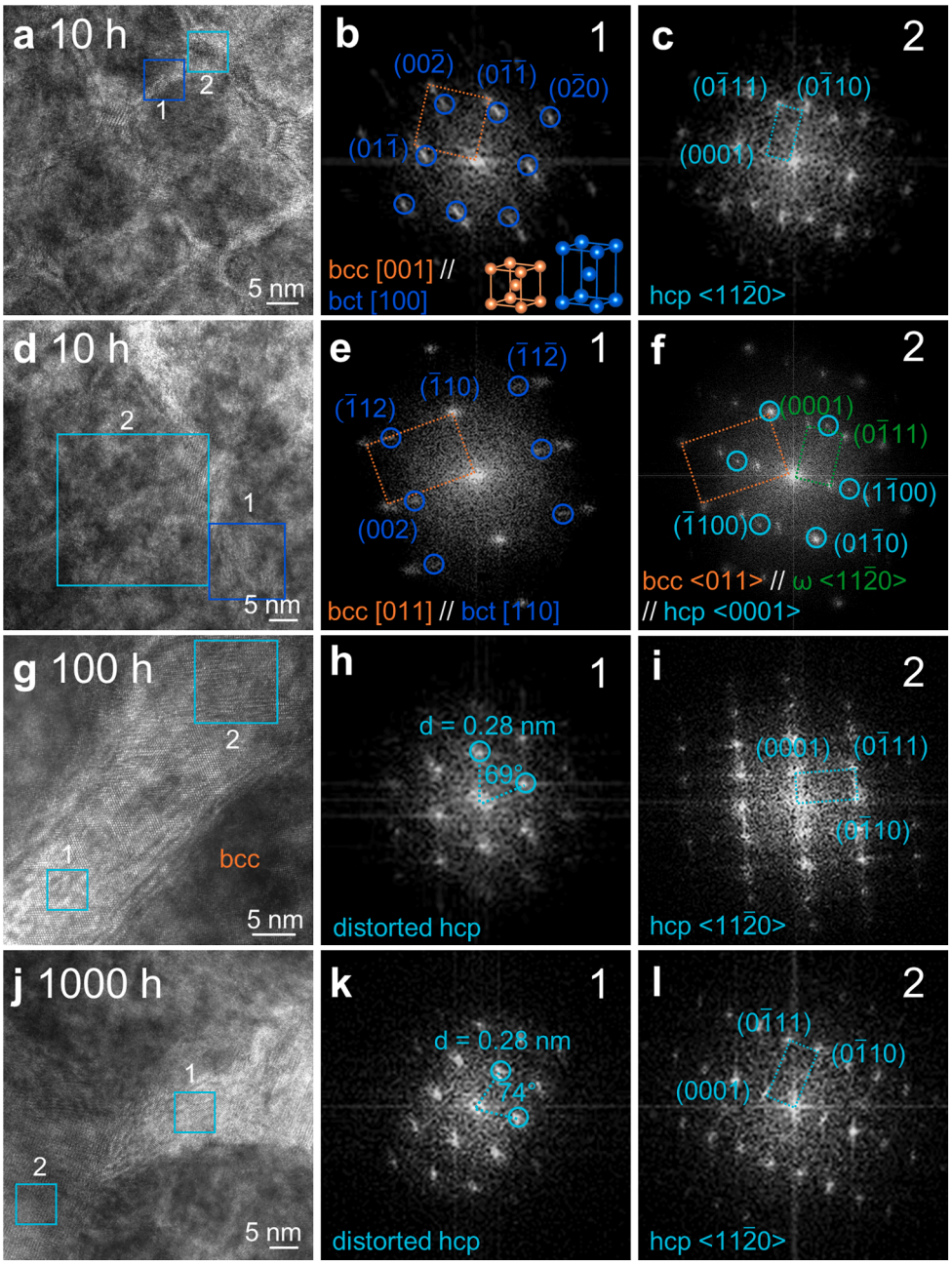

Fig. 2. High-resolution transmission electron microscopy (HRTEM) images of the initially single-phase bcc HfNbTaTiZr alloy aged for (a, d) 10 h, (g) 100 h, and (j) 1000 h are shown in the first column. Fast Fourier Transform (FFT) images are displayed in the second and third columns. Those in (b, e, h, and k) and (c, f, i, and l) were recorded from the rectangular regions 1 and 2 marked in the first column, respectively. The unit cells of bcc and bct structures are illustrated in (b).

In contrast, the bct, ω, and distorted hcp phases are metastable phases, whose formation is likely related to the anisotropy of the matrix phase, similar to those in the Ti-based alloys [43–46].

APT measurements were carried out to investigate elemental partitioning in the different phases. The compositions of all the phases in HfNbTaTiZr in the as-received condition and aged at 500 °C for 1 h up to 1000 h are listed in Table S1. The error ranges provided for the elemental concentrations denote the standard deviations. It is worth noting that according to the APT measurements, HfNbTaTiZr contains ~0.5 at.% O in the as-received state, which mainly originated from the raw metals used for casting [47,48]. Atom maps of HfNbTaTiZr aged for 1 h, 10 h, 100 h, and 1000 h, are shown in Figs. 3a to 3d, respectively.

A binomial analysis [49,50] was performed to investigate elemental distributions in the 1-h aged HfNbTaTiZr. The curves of frequency distributions obtained experimentally nearly overlap with the theoretical randomized data in Fig. 3e, suggesting a random distribution of the elements as also observed in Fig. 3a.

After aging for 10 h (Fig. 3b), distinct phases are detected, the compositions of which are displayed in Fig. 3f. Blue Zr-rich channels delineated by 27 at.% Zr isoconcentration surfaces are observed in Fig. 3b These correspond to the bct channels observed by TEM in Figs. 1b and 2a. At and near the channel nodes, green ~10-nm particles containing ~40 at.% Zr (Fig. 3f) and ~10-nm Ti-rich clusters, shown by 26 at.% Ti isoconcentration surfaces in Fig. 3b, are detected. These correspond to the hcp and ω particles, respectively, as identified by TEM in Figs. 1d and 2f. While the bct channels and hcp phase are both enriched in Zr and Hf, the hcp phase has a higher Zr concentration and lower Nb and Ta contents, see Fig. 3f. In contrast, the ω phase is enriched in Ti

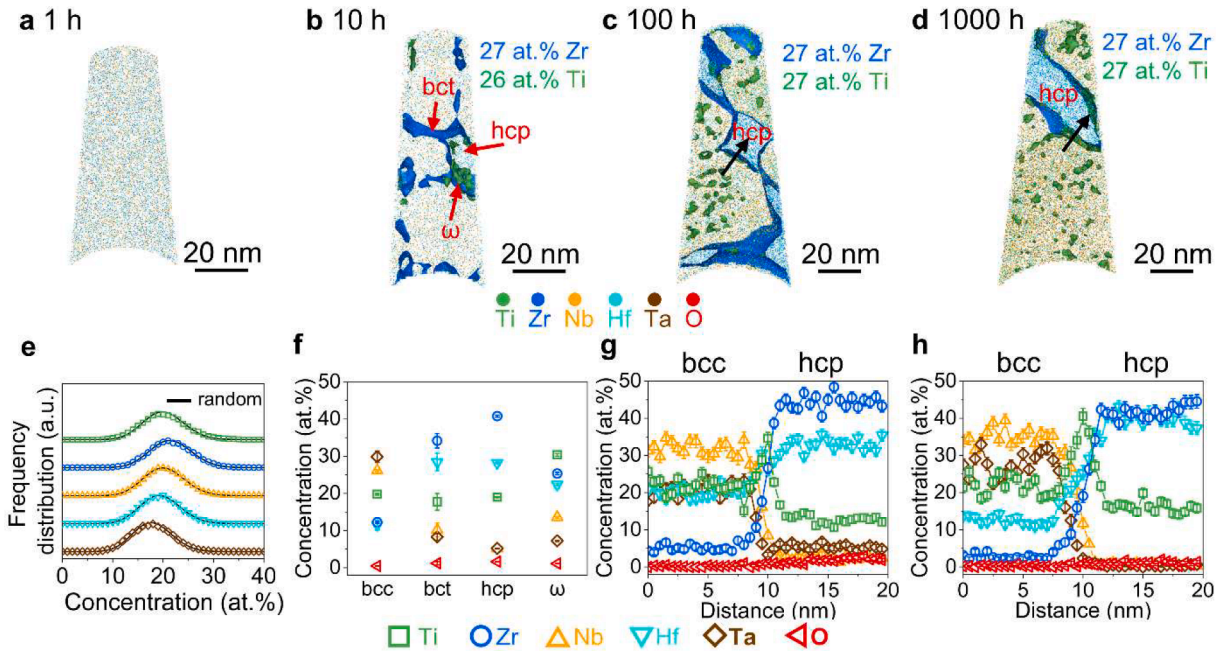

Fig. 3. Atom maps overlaid with Ti and Zr isoconcentration surfaces of the APT reconstruction cross-section views of HfNbTaTiZr aged at 500 °C for (a) 1 h, (b) 10 h, (c) 100 h, and (d) 1000 h. (e) Frequency distribution analysis of the alloying elements of the 1-h aged state. (f) Compositions of different phases observed in the 10-h aged alloy. (g) and (h) 1D concentration profiles from bcc to hcp phases along the arrows in (c) and (d), respectively.

((30.4 ± 0.4) at.%), and to a lesser extent in Zr and Hf ((25.7 ± 0.4) at.% Zr, (21.4 ± 0.4) at.% Hf). As the fast-diffusing hcp-stabilizers diffuse to the secondary phases, the bcc matrix is depleted in these elements and correspondingly enriched in Nb and Ta, which diffuse at a slower rate [51]. O preferentially partitions to the hcp phase followed by the bct channels and ω particles.

With increasing aging time from 100 to 1000 h (Figs. 3c and 3d), the Zr-O-rich (and Nb-Ta-poor) hcp regions within channels and at channel nodes progressively grow, and the composition of the latter does not differ significantly from the former. One-dimensional (1D) concentration profiles from the bcc matrix to hcp phase were recorded along the arrows shown in Figs. 3c and 3d and the obtained results are presented in Figs. 3g and 3h, respectively. Here, Ti segregation is evident at the interfaces between Nb-Ta-rich bcc and Zr-Hf-rich hcp, see green peak in the middle of the concentration profiles. Hf diffuses into hcp more slowly than Zr, as evidenced by the delayed increase in Hf concentration in hcp during its growth from 100 to 1000 h. Moreover, as the Nb-Ta-poor hcp phase grows between 100 and 1000 h, Nb and Ta are rejected into the bcc matrix where their concentrations increase in the bcc matrix (compare Figs. 3g and 3h). In addition, nanosized Ti-rich clusters form in the bcc matrix after 100 h (see green particles marked with 27 at.% Ti isoconcentration surfaces in Fig. 3c) and their size remains nearly constant upon aging from 100 to 1000 h (Fig. 3d). The center of these clusters is enriched in Ti and this element becomes progressively replaced by Nb and Ta as one moves toward their edges, according to the proxigrams shown in Fig. S8.

3.2. Phase stability of HfNbTaTiZr-3O during aging at 500 °C

SEM characterization of HfNbTaTiZr-3O after different heat treatments is displayed in Fig. S1. Like HfNbTaTiZr, nanosized features are found within grains after sufficient aging time in HfNbTaTiZr-3O. The microstructural evolution of HfNbTaTiZr-3O investigated by TEM along $<001>_{bcc}$ ZAs is displayed in Fig. 4. There are no diffraction spots other than those of a bcc solid solution in the SADP in the as-received and 1-h aged states, but faint diffuse streaks around the bcc spots are observed in Fig. 4a. DF TEM images taken from the white circled regions numbered 1 and 2 in Fig. 4a, are shown in Figs. 4b and 4c, respectively, where a network of perpendicular channels can be observed. In contrast to HfNbTaTiZr, in which the diffuse streaks strongly weakened during aging, these streaks are still clearly visible in HfNbTaTiZr-3O even after aging for 100 h, see Fig. 4g. From the white circled regions in Figs. 4d and 4g, the DF TEM images in Figs. 4e and 4h were taken, respectively, to investigate the evolution of the channels with time in HfNbTaTiZr-3O. Upon aging between 10 and 100 h, the bct channels slightly thicken from (2.1 ± 0.5) nm to (2.5 ± 1.7) nm and the inter-channel distance increases from (13.3 ± 3.4) nm to (18.2 ± 5.1) nm, indicating that some bct channels have dissolved to enable the formation of a coarser microstructure. Compared to HfNbTaTiZr, the bct channels in HfNbTaTiZr-3O are thinner, i.e., (2.7 ± 0.9) nm in HfNbTaTiZr and (2.1 ± 0.5) nm in HfNbTaTiZr-3O both aged for 10 h.

In HfNbTaTiZr-3O, hcp particles are also observed mainly at channel nodes, as shown in the DF TEM images (Figs. 4f and 4i), for which the blue circled hcp spots in Figs. 4d and 4g were selected. The size of hcp particles at the nodes in HfNbTaTiZr-3O increases from (2.9 ± 0.7) nm to (3.4 ± 0.9) nm, and the number of particles increases from 3333 to 3556 μm^{-2} between 10 and 100 h.

After aging HfNbTaTiZr-3O for 1000 h, sharp $<11\bar{2}0>_{hcp}$ variant diffraction spots are observed in Fig. 4j without any discontinuous diffraction rings, in contrast to HfNbTaTiZr (see rings highlighted by blue double arrows in Fig. 1j). Compared to the 100-h heat treatment, the distance between the channels further decreases after aging for 1000 h to (61.0 ± 18.4) nm and the thickness of the channels increases to (27.1 ± 8.6) nm, see Figs. 4h and 4k. The hcp phase at the nodes grows (mean size: (27.6 ± 10.1) nm) and its number density decreases from 3600 to 173 μm^{-2} as the aging time increases to 1000 h, revealed by the DF micrograph in Fig. 4l. In short, the microstructure of the 1000-h aged HfNbTaTiZr-3O is finer than that of the HfNbTaTiZr aged under the same condition, i.e., the sizes of the node hcp phase and the channels are smaller in HfNbTaTiZr-3O compared to those in HfNbTaTiZr.

To elucidate the nanoscale structural evolution in HfNbTaTiZr-3O during aging from 10 h to 1000 h, HRTEM investigations along $<001>_{bcc}$ ZAs were performed, see Fig. 5. The structural features in HfNbTaTiZr-3O are similar to those in HfNbTaTiZr, but a few differences are worth mentioning. First, the diffraction patterns of a bct structure

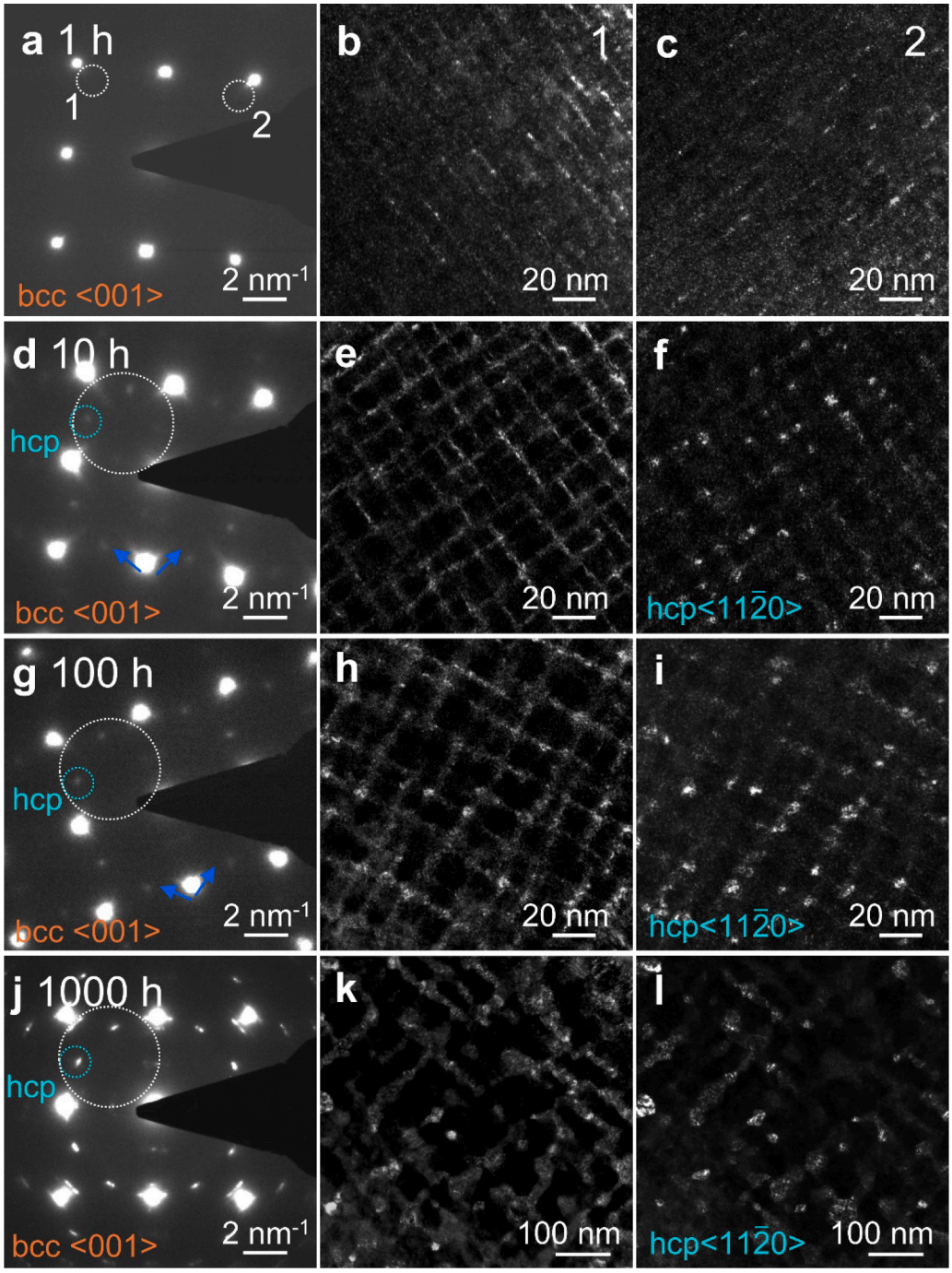

Fig. 4. Evolution of microstructures in the initially single-phase bcc HfNbTaTiZr-3O alloy during aging at 500 °C for (a-c) 1 h, (d-f) 10 h, (g-i) 100 h, and (j-l) 1000 h. SADPs recorded along $<001>_{bcc}$ ZAs are shown in the first column. The DF TEM images in (b) and (c) were acquired from the white circles numbered 1 and 2 in (a), respectively. From the white and blue circled regions of the SADPs in (d, g, and j), DF images were recorded, which are displayed in the second and third columns of the corresponding states. For more details see text.

identified by the FFT images (Fig. S6) are found in the 10-h and 100-h aged HfNbTaTiZr and HfNbTaTiZr-3O. This indicates that the bct channels are preserved up to 100 h, resulting in the diffused streaks in Figs. 5b and 5e. In contrast, the bct channels have either dissolved or transformed to the hcp phase in HfNbTaTiZr after aging for 100 h (Fig. 2*g*). Second, the hcp phase within channels in the 1000-h aged HfNbTaTiZr-3O does not exhibit any distortions but corresponds to an ideal hcp phase, see FFT along $<10\bar{1}1>_{hcp}$ ZA in Fig. 5h taken from frame number 1 in Fig. 5*g*. In contrast, the ideal hcp phase did not form in HfNbTaTiZr; the distorted hcp phase was observed within channels after aging for 1000 h (Figs. 2j and 2k).

TEM characterization was also carried out along $<011>_{bcc}$ ZAs to investigate the temporal evolution of the ω phase. Figs. 6a-c exhibit SADPs of HfNbTaTiZr-3O aged at 500 °C for 10 h, 100 h, and 1000 h, respectively. The corresponding DF images of ω particles are shown in Figs. 6d-f. Due to the low volume fraction of the ω phase, its diffraction spots are faint after aging for 10 h (Fig. 6a). As aging time increases to 100 h, the ω spots become more intense due to the increase in number density from 37 to 264 μm^{-2} and the increase in mean size from (6.0 ± 2.6) nm to (9.4 ± 2.1) nm of the ω particles. For the 1000-h aged sample (Fig. 6f), a few large (41.1 ± 10.6) nm ω particles are still present in HfNbTaTiZr-3O, while this phase was completely absent in HfNbTaTiZr

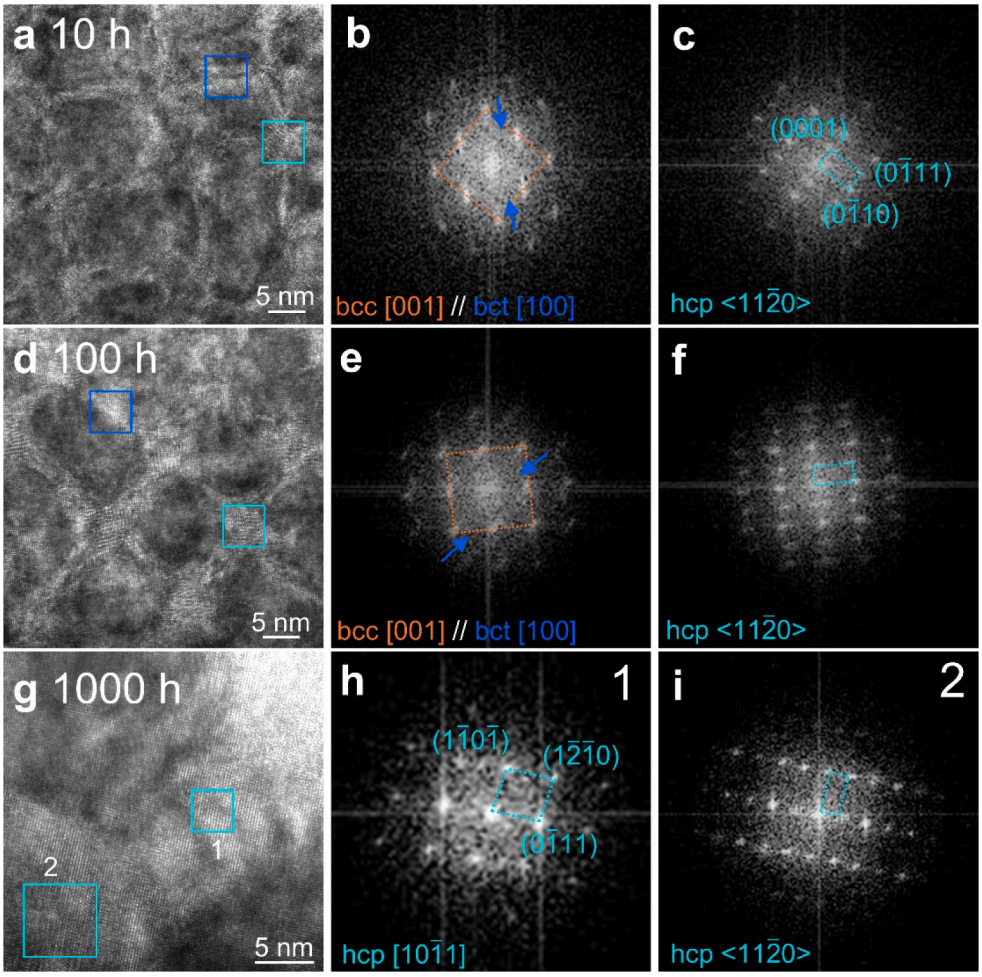

Fig. 5. HRTEM images along $<001>_{bcc}$ ZAs of the HfNbTaTiZr-3O aged for (a) 10 h, (d) 100 h, and (g) 1000 h. FFT images of the regions marked with dark and light blue frames in (a, d) are shown in (b, e) and (c, f) and reveal the presence of bct and hcp phases oriented along $[100]_{bct}$ and $<11\bar{2}0>_{hcp}$ ZAs, respectively. (h) and (i) FFT images of the framed regions numbered 1 and 2 in (g), showing an hcp channel along $<10\bar{1}1>_{hcp}$, and an hcp node along $<11\bar{2}0>_{hcp}$ ZAs, respectively.

under the same aging condition.

The lattice parameters of the ω phase in HfNbTaTiZr-3O were determined from the SADPs and the results are listed in Table 1. As aging time increases, the *a* axis continuously increases while the *c* axis becomes shorter.

The elemental partitioning among the phases in HfNbTaTiZr-3O during aging at 500 °C from 1 to 1000 h is shown as atom maps overlaid with isoconcentration surfaces in Figs. 7a-d, the corresponding phase compositions are summarized in Table S2 and those after aging for 10 and 100 h are shown in Figs. 7f and 7*g*, respectively.

After 1 h (Fig. 7a), blue Zr-rich channels, delineated by 27 at.% isoconcentration surfaces, are starting to form, consistent with the TEM observations in Figs. 4b and 4c. The frequency distribution analysis in Fig. S9 shows that Ti, Zr, Nb, and Ta are not homogeneously distributed as the experimental curves do not match perfectly with the randomized data. A slab-shaped region of interest (ROI) with a 5-nm thickness, marked with a red dashed line in Fig. 7a, is magnified on the left of Fig. 7e, where the red, green, and blue isoconcentration surfaces correspond to O at 3.1 at.%, Ti at 24.5 at.%, and Zr at 27 at.%, respectively. The red O-rich and blue Zr-rich regions are found to be either superimposed or close to each other, indicating that O might favor Zr segregation. In addition, Ti-rich clusters are often located in the vicinity of the Zr-rich clusters. In contrast, Nb and Ta are enriched within the cuboids between the channels as shown in the two-dimentional (2D) concentration map of Nb+Ta on the right side of Fig. 7e.

After 10 h, a well-defined network of Zr-rich channels has formed (Fig. 7b), which becomes thicker with increasing aging time (see Figs. 7c and 7d). For aging durations between 10 and 1000 h, green ω particles delineated by the 27 at.% Ti isoconcentration surfaces, decorate the channel nodes. The elemental partitioning behavior is similar to the one in HfNbTaTiZr, as seen by comparing Figs. 7f and 7*g* with Fig. 3f. As the aging time increases from 10 to 100 h, Zr, Hf, and O concentrations in the bct channels, hcp phase, and ω phase slightly increase, while the concentrations of these elements in the bcc matrix keep decreasing. In addition, Nb and Ta are gradually rejected from the ω phase, and its Ti concentration increases with time.

In contrast to HfNbTaTiZr, where the ω particles dissolve between 10 and 100 h, they are observed in HfNbTaTiZr-3O, even after 1000 h, indicating that O may stabilize this phase. Consistent with this hypothesis, the O concentration in the ω phase gradually increases during aging from 3.0 at.% after 10 h to 7.8 at.% O after 1000 h, Table S2. Meanwhile, the O content in the hcp phase also increases from 4.6 to 6.8 at.%. To investigate the elemental partitioning across bcc/ω/hcp phase boundaries, a 1D concentration profile was obtained along the arrow in Fig. 7d The result in Fig. 7h shows a Ti-rich region close to the bcc/ω interface and that indeed more O is present in the ω and hcp phases than in the bcc matrix (~0.7 at.%).

3.3. Mechanical properties

To investigate the effects of O and the influence of the nanoscale secondary phases on strength and ductility, mechanical tests were

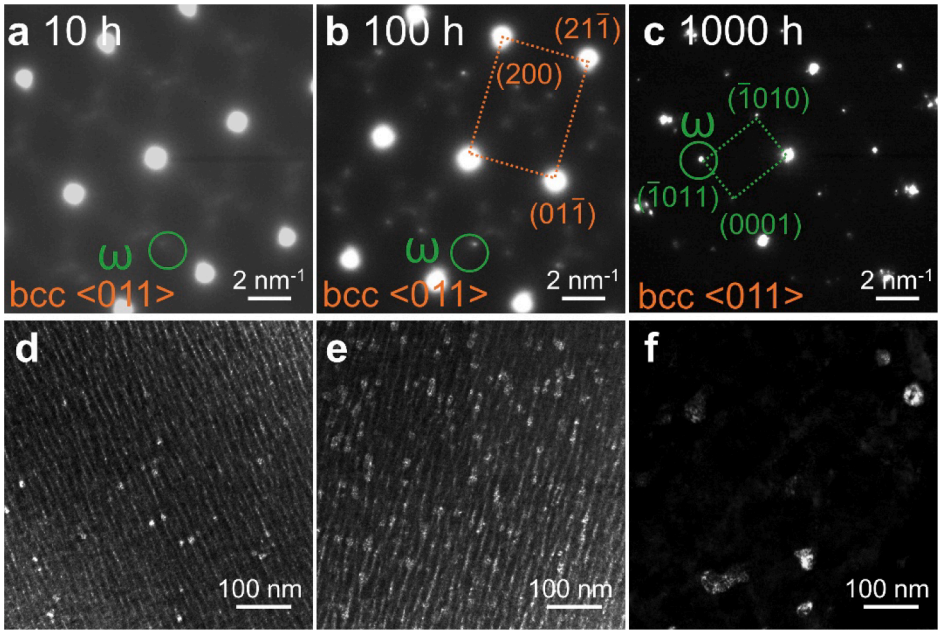

Fig. 6. TEM characterization of the ω phase in the HfNbTaTiZr-3O alloy aged for 10 h, 100 h, and 1000 h, and displayed in the first, second, and third columns, respectively. (a-c) SADPs along $<011>_{bcc}$ ZAs where the green circles highlight the diffraction spots of the ω phase that were selected to record the corresponding DF TEM images shown in (d-f).

Table 1
Lattice parameters of the ω phase in the HfNbTaTiZr-3O after different aging times at 500 °C.

10 h	100 h	1000 h
$a = 0.47 \pm 0.01$ nm $c = 0.33 \pm 0.01$ nm	$a = 0.49 \pm 0.01$ nm $c = 0.31 \pm 0.01$ nm	$a = 0.50 \pm 0.01$ nm $c = 0.30 \pm 0.01$ nm

performed on the HfNbTaTiZr and HfNbTaTiZr-3O after different heat treatments. The engineering tensile stress-strain curves of the as-received HfNbTaTiZr-3O (red curve) and the HfNbTaTiZr in the as-received (black) and 10-h aged (blue) conditions are shown in Fig. 8a. In the as-received state, the single-phase bcc HfNbTaTiZr solid solution has a yield strength of (960 ± 60) MPa and a strain to fracture of (24 ± 8) %, whereas the bcc HfNbTaTiZr-3O is brittle and fails during elastic deformation at ~300 MPa, see inset of Fig. 8a. After aging for 10 h, HfNbTaTiZr fractures above 1200 MPa before yielding, indicating that the formation of the nanosized secondary phases after aging for 10 h at 500 °C strengthens and embrittles the alloy.

From the ruptured tensile specimens, the fracture surfaces were systematically investigated, Figs. 8b-e. The dimples observed on the fracture surface of the as-received HfNbTaTiZr in Fig. 8b, are typical of ductile failure. In contrast, the fracture surface of the bcc HfNbTaTiZr-3O (as-received state, Fig. 8c) is a typical feature of brittle failure with a mixture of transgranular and intergranular fracture, similar to the observations of Dobbelstein et al. [52] in a HfNbTaTiZr-1.9O-0.8N produced by additive manufacturing. This embrittlement may be related to O-segregation at grain boundaries [53–55], which may favor grain boundary decohesion and thus crack initiation. However, further experiments, beyond the scope of this paper, involving systematic investigations on grain boundary segregations, are required to support or refute this hypothesis.

In HfNbTaTiZr aged for 10 h (Figs. 8d and 8e), the fracture surface reveals three distinct features, which are also typically observed in Ti-alloys [56,57]: (1) cracks at some grain boundaries (e.g., large crack in the middle of Fig. 8e), (2) small dimples within grains (top left region of Fig. 8e), and (3) transgranular fracture where parallel bands of bright and aligned particles can be observed (marked by the arrow in the bottom right of Fig. 8e). This heterogeneous fracture surface may well reflect the microstructural heterogeneities present after aging, i.e., the formation of hcp phase at grain boundaries may trigger intergranular fracture as reported by Schuh et al. [10] and Dobbelstein et al. [52], while the presence within grains of a network of bct channels as well as ω and hcp particles at channel nodes may promote transgranular failure, as reported by Yasuda et al. [13].

Microhardness tests were performed within grains to investigate the influence of microstructure evolution on the hardening effect in HfNbTaTiZr and HfNbTaTiZr-3O. For a given heat treatment, HfNbTaTiZr-3O (red data points in Fig. 9a) is systematically harder than HfNbTaTiZr (blue) by ~150 HV0.05, but both alloys show a similar hardening evolution during aging. The hardness increases rapidly during the first 10 h and reaches a maximum after ~100 h, probably due to the formation of nanoscale phases, including bct channels, hcp at channel nodes, and ω particles. Between 100 and 1000 h, a slight decrease in hardness is observed (Fig. 9a), most probably due to the microstructure coarsening (e.g., compare Figs. 7c and 7d), driven by the reduction in the overall interfacial energy [58]. The coarsening leads to a reduction in the number density of interfaces that act as barriers to dislocation motion, resulting in the slight reduction in hardness between 100 and 1000 h. Interestingly, the peak hardness is more pronounced in HfNbTaTiZr-3O than in HfNbTaTiZr. This may reflect the effect of ω particles on strength after aging for 100 h, but it could also reflect the higher number density in HfNbTaTiZr-3O compared to HfNbTaTiZr (e.g., compare Figs. 1h, 1k and 4h, 4k).

To further study the impact of nanoscale secondary phases on the deformation behavior, micropillar compression tests were conducted in $<001>_{bcc}$-oriented grains. The obtained engineering stress-strain curves of HfNbTaTiZr and HfNbTaTiZr-3O after different heat treatments are shown in Fig. 9b as dashed and solid lines, respectively. The evolution of the yield strength with aging duration (see Table 2) is like that of the microhardness in Fig. 9a, i.e., for a given heat treatment, the flow stress at a given strain is systematically higher for HfNbTaTiZr-3O than for HfNbTaTiZr. In the as-received state with a bcc solid solution microstructure, this difference suggests a stronger interstitial solid solution strengthening by O atoms in HfNbTaTiZr-3O, consistent with previous studies [19]. In both alloys, the stress-strain curves of the as-received

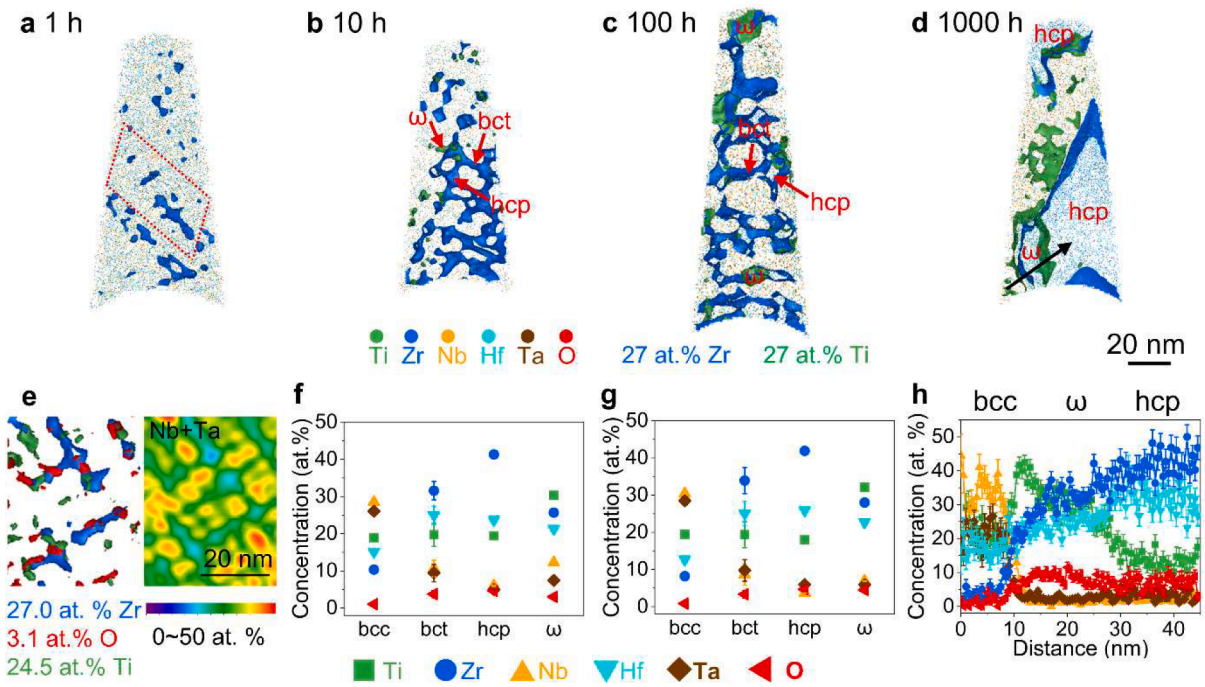

Fig. 7. Nanoscale characterization of the HfNbTaTiZr-3O aged up to 1000 h at 500 °C. Atom maps overlaid with Ti and Zr isoconcentration surfaces (27 at. % each) of the APT reconstruction cross-section views for aging times of (a) 1 h, (b) 10 h, (c) 100 h, and (d) 1000 h. (e) Iso-concentration surfaces of Zr at 27.0 at.%, O at 3.1 at.%, and Ti at 24.5 at.%, and 2D concentration map of Nb+Ta in an ROI with a thickness of 5 nm highlighted with the red dashed lines in (a). (f) and (g) Compositions of different phases observed in the 10-h and 100-h aged specimens, respectively. (h) 1D concentration profiles from bcc through ω to hcp phases along the arrow in (d).

and 1 h-aged condition approximately overlap, consistent with the fact that secondary phases have not formed yet, see Fig. S2c and Fig. 4a. With increasing aging time to 10 h, nanosized bct, hcp, and ω phases have formed within grains, where they impede the movement of dislocations, resulting in strengthening. The yield stress then reaches a maximum after aging for 100 h due to an increase in the volume fraction of secondary phases (compare Figs. 1b and 1c). After aging for 1000 h, the microstructure has significantly coarsened, resulting in a decrease of the yield stress by ~100 MPa, see Table 2. Finally, the higher strength of HfNbTaTiZr-3O compared to HfNbTaTiZr after aging can be attributed to the higher number density of the secondary phases. Figs. 9c and 9d show the micropillars of the 10-h aged HfNbTaTiZr and HfNbTaTiZr-3O after compression tests, respectively. Slip planes along different orientations were observed, demonstrating dislocation activity in both alloys, consistent with Ref. [59].

4. Discussion

4.1. Phase formation sequence

Our TEM and APT investigations provide new insights into the role of O in the phase stability of the HfNbTaTiZr alloy upon aging at 500 °C, as schematically illustrated in Fig. 10. In HfNbTaTiZr (Fig. 10a), ~2.7-nm thick bct channels enriched in Zr and Hf form along $<001>_{bcc}$ crystallographic directions in the bcc matrix. No preferential orientation among the three inequivalent orientation relationships between bcc and bct was found, as indicated by the similar interdistance between the channels, size (Fig. S4), and composition of the channels (Fig. S10) along the three $<001>_{bcc}$ directions. The nodes of the channels have higher concentrations of Zr and Hf, facilitating the formation of hcp phase with Ti-rich ω particles at bcc/hcp interfaces. Further aging leads to complete dissolution of the ω phase and partial dissolution of the bct channels. The residual bct channels transform into a distorted Zr-Hf-rich hexagonal phase, which is thicker than the radius of the initial hcp particles.

For HfNbTaTiZr-3O (Fig. 10b), O promotes the formation of finer bct channels (~2.1-nm thick) due to the more pronounced Zr segregation at the channels compared to HfNbTaTiZr. As the channel nodes are enriched in Zr and O, they constitute favorable sites for the formation of hcp particles. Moreover, Ti-rich ω particles are found close to bcc/hcp interfaces. As aging proceeds, the bct channels dissolve partially, and more channel nodes transform to hcp. Meanwhile, the number density of ω particles at bcc/hcp interfaces and their mean size increase, indicating the stabilization of this phase, associated with the partitioning of O and Ti towards ω particles and the rejection of Nb and Ta to the cuboidal bcc regions. A longer aging time leads to phase transformation from bct to hcp and partial dissolution of ω phase. The final microstructure is composed of bcc, hcp, and ω with the sequence of O contents in the three phases being O(ω) > O(hcp) > O(bcc).

The volume fractions of different phases in HfNbTaTiZr and HfNbTaTiZr-3O were measured from TEM DF images using ImageJ software, as shown in Figs. 10c and 10d. The total amount of O in the two alloys were estimated by using the APT-compositions and molar fractions of different phases, converted from volume fractions. As shown in Fig. S13, with increasing aging duration, the total O content in the alloys does not vary significantly from their initial conditions, indicating that the observed phase formation sequence is not influenced by the possible O ingress during aging.

It is noteworthy that a recent work [14] reports the formation of an hcp2 phase with a smaller c/a ratio compared to the hcp1 phase in the nanocrystalline HfNbTaTiZr alloy during aging at 500 °C, while only one type of hcp phase (Zr-Hf-rich hcp) is observed in our present work. The thermodynamic modeling shows an hcp2 phase is stable at temperatures lower than 500 °C [10]. The formation of the hcp2 phase at 500 °C in Ref. [14] might be affected by the severe plastic deformation applied to the alloy, which introduced a high density of defects and lattice strain, stabilizing hcp2 phase. In our study, however, the grain size of the initially bcc HfNbTaTiZr alloy is much larger. The grain boundaries and the other defects do not significantly impact the phase stability. The

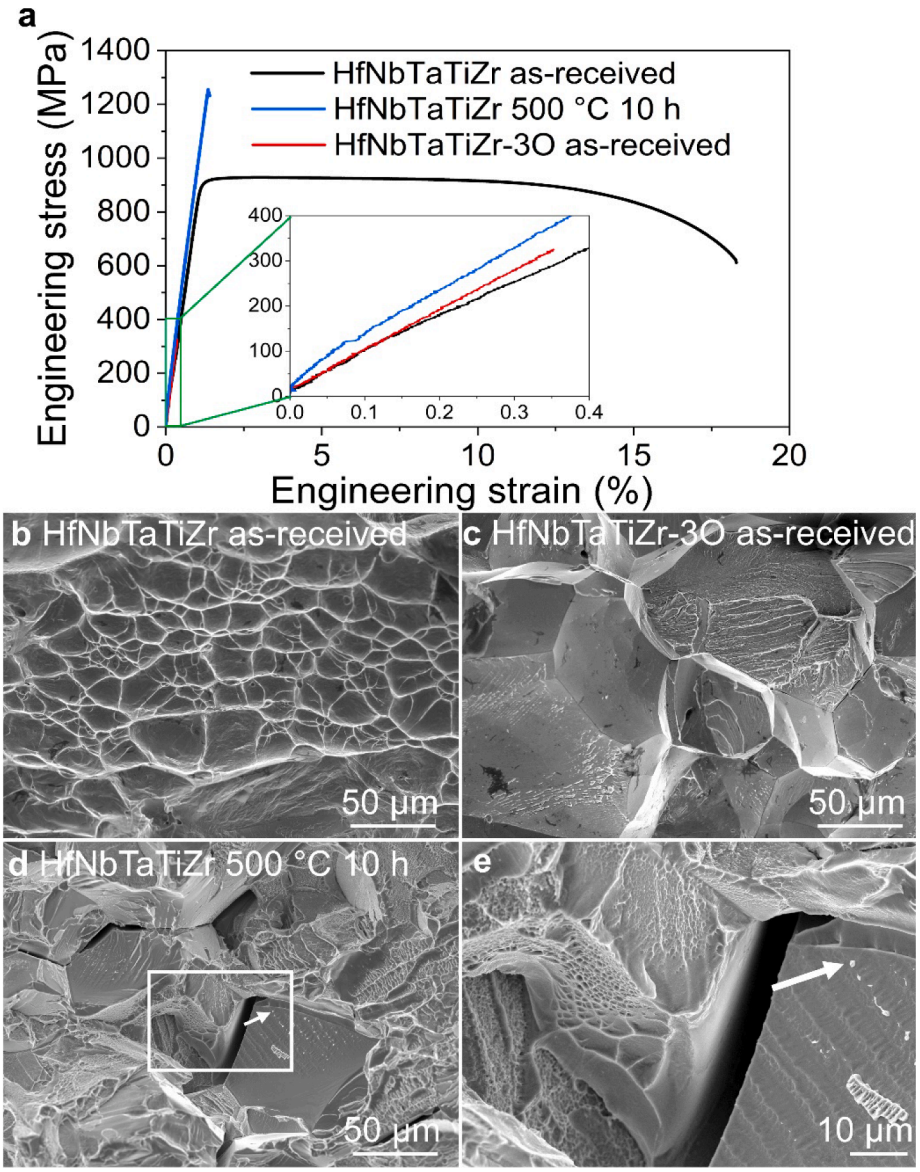

Fig. 8. Tensile tests and fractography of the HfNbTaTiZr and HfNbTaTiZr-3O in the as-received and aged states. (a) Engineering stress-strain curves of the HfNbTaTiZr (black curve) and HfNbTaTiZr-3O (red) in the as-received condition as well as HfNbTaTiZr after aging at 500 °C for 10 h (blue). Fracture surfaces of (b) as-received HfNbTaTiZr, (c) as-received HfNbTaTiZr-3O, and (d) HfNbTaTiZr aged at 500 °C for 10 h. The region marked with a white frame in (d) is magnified in (e).

observed bcc and hcp phases after 1000 h of aging and the absence of hcp2 phase in the current work are consistent with the equilibrium phases at 500 °C calculated in Thermo-Calc with TCTI6 database (Figs. S16a and b). This simulation qualitatively reproduced the phase stabilities reported in Refs. [8,10] by using TCHEA1 and TCHEA4, respectively. We found that O preferentially dissolves into the hcp phase in comparison to bcc (Table S6), in line with the APT characterization. By suspending the hcp phase, the ω phase is found in HfNbTaTiZr at temperatures < 325 °C (Fig. S16c), lower than 500 °C. This could be attributed to the extended stability of ω due to the addition of O, similar to that in the Ti-based alloy [28]. Although the metastable phases form during aging in the two alloys, the total molar Gibbs free energy of the system decreases with increasing aging time, towards a state closer to the equilibrium (Fig. 10e, for the details of the calculation, see Supplementary Material section G).

4.2. Formation of bct channels and lattice relaxation

The perpendicular Zr-Hf-rich channels along $<001>_{bcc}$ directions forming a network were evidenced in both alloys (Figs. 1 and 4). To understand their formation mechanism, detailed compositional analyses were performed. The 2D concentration maps of Zr from a 5-nm thick ROI in HfNbTaTiZr aged for 1, 10, and 100 h are displayed in Figs. 11a-c, which show channel growth and a gradual change in Zr partitioning between matrix and channels as time increases from 1 to 100 h. From the 35-nm long arrows parallel to *a* $<001>_{bcc}$ direction and crossing multiple channels and cuboids in Figs. 11a-c, the 1D concentration profiles of Zr shown in Fig. 11d were recorded (1 h: orange curve, 10 h: red curve, 100 h: blue curve), while the corresponding profiles of the other elements are shown in Fig. S11 for the sake of completeness. The Zr concentration profiles in Fig. 11d reveal that the amplitude of the compositional modulation of Zr wave increases with time, while the number of wave maxima per unit length decreases. These characteristics suggest that spinodal decomposition [60] can be a possible formation

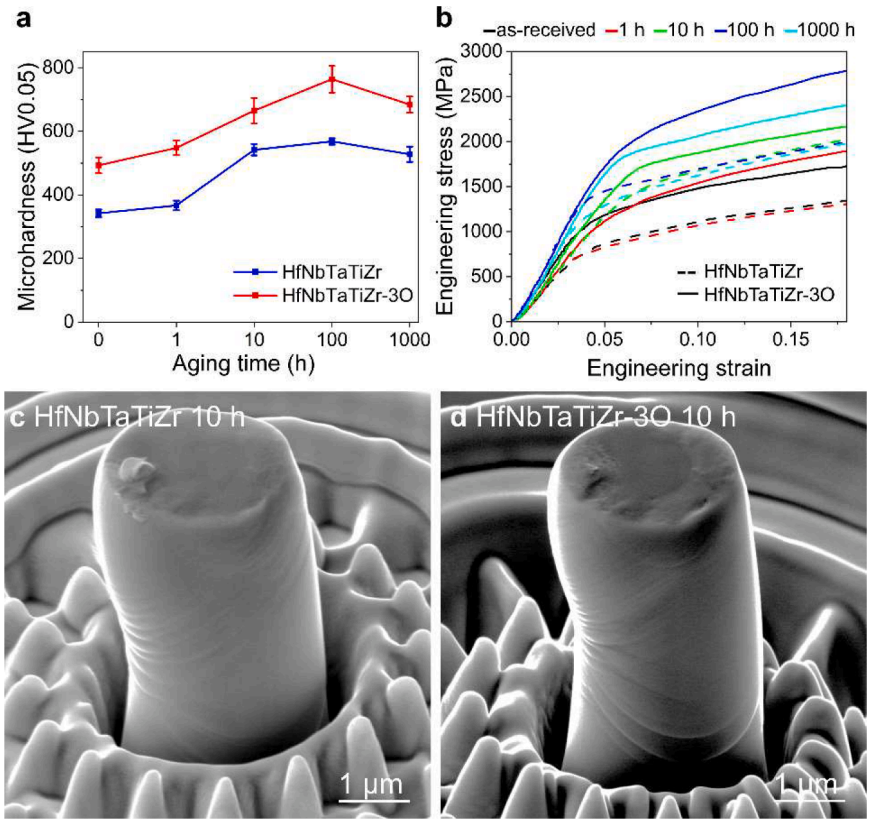

Fig. 9. Micro-mechanical tests performed in the interior of grains of the HfNbTaTiZr and HfNbTaTiZr-3O under as-received states and aged at 500 °C for different times. (a) Temporal evolution of microhardness. (b) Engineering stress-strain curves of micropillars of the HfNbTaTiZr (dashed curves) and HfNbTaTiZr-3O (solid curves) aged for different durations. (c) and (d) SEM images of the deformed pillars of the 10-h aged HfNbTaTiZr and HfNbTaTiZr-3O, respectively. Note the presence of slip traces in both cases.

Table 2
Yield strengths (MPa) of micropillars of HfNbTaTiZr and HfNbTaTiZr-3O under different conditions.

	as-received	1 h	10 h	100 h	1000 h
HfNbTaTiZr	670 ± 30	560 ± 30	1140 ± 30	1170 ± 30	1070 ± 30
HfNbTaTiZr-3O	860 ± 30	870 ± 30	1150 ± 30	1600 ± 50	1490 ± 30

mechanism for the bct channels. In a recent study [16] combining APT and thermodynamic modeling, hydrogen was found to assist the spinodal decomposition of HfNbTaTiZr at 500 °C (between 0.5 to 2 h). In the present work, O may play a similar role, since it is present in both HfNbTaTiZr and HfNbTaTiZr-3O. In the case of a spontaneous spinodal decomposition in both alloys, the bcc phase would be intrinsically unstable at 500 °C [61] and the decomposition would occur in the early stages of aging (before 10 h). With increasing time, compositional modulation magnitude is enhanced with the increased chemical enrichment of Zr and Hf. Due to the larger atomic radii of Hf and Zr compared to the other elements ($r_{Ti} = 176$ pm, $r_{Zr} = 206$ pm, $r_{Nb} = 198$ pm, $r_{Hf} = 208$ pm, $r_{Ta} = 200$ pm [62,63]), the lattice parameters of the regions with compositional modulation increase, causing lattice misfit between the modulations and the bcc phase. As shown in the first stage in Fig. 10b, the compositional modulations, spaced at regular distances, are aligned along one of the $<001>_{bcc}$ crystallographic directions, which is the modulation wave direction. Along the other two $<001>_{bcc}$ orientations, perpendicular to the modulation wave direction, the volume of bcc phase is larger than the bcc phase between two modulated peaks. Consequently, the elastic strain due to lattice misfit at the bcc/modulation interfaces parallel to the modulation wave direction can be relaxed, but is maintained at the interface perpendicular to the modulation propagation. This anisotropic strain contributes to the tetragonal distortion of the bcc phase [64,65], leading to the formation of bct structure. The phase formation sequence with spinodal decomposition followed by hcp precipitation in the HfNbTaTiZr alloy under compression at 600 °C has been reported recently [66], where the deformation-induced strain and stress play a dominated role in phase transformation, accompanied by the non-BOR relationship between bcc and hcp. In contrast, the classic BOR is found in our diffusion-controlled phase transitions. Therefore, it cannot be concluded that the same sequence is applied to the aging behavior of the HfNbTaTiZr alloy at 500 °C in the present study. A formation mechanism of nucleation and growth (as opposed to a spinodal decomposition) of bct phase cannot be excluded, as the observed increase in compositional modulation with time in the present study is not significant considering the error bars in Fig. 11d. Here, the interface region is rather sharp, which differs from the observations of Wu et al. [16]. As the APT measurements do not provide crystal structure information in this case, some high peaks in Fig. 11d (e.g., the peak at ~25 nm) could correspond to an hcp particle. Furthermore, it is the value of $\frac{\partial^2 G}{\partial c^2}$ [67] (where G and c are the Gibbs free energy and the elemental concentration, respectively) that determines whether spinodal decomposition occurs. Therefore, a careful thermodynamic re-assessment of the system (under the influence of O) should be carried out in the future, but such a study is beyond the scope of the present article. If the formation of bct were to follow a nucleation mechanism, the bcc phase in HfNbTaTiZr would be metastable and the nucleation of bct nuclei with a critical size would require thermal activation [67]. In addition to the phase stability determined by thermodynamic considerations, the observed tetragonality could also originate

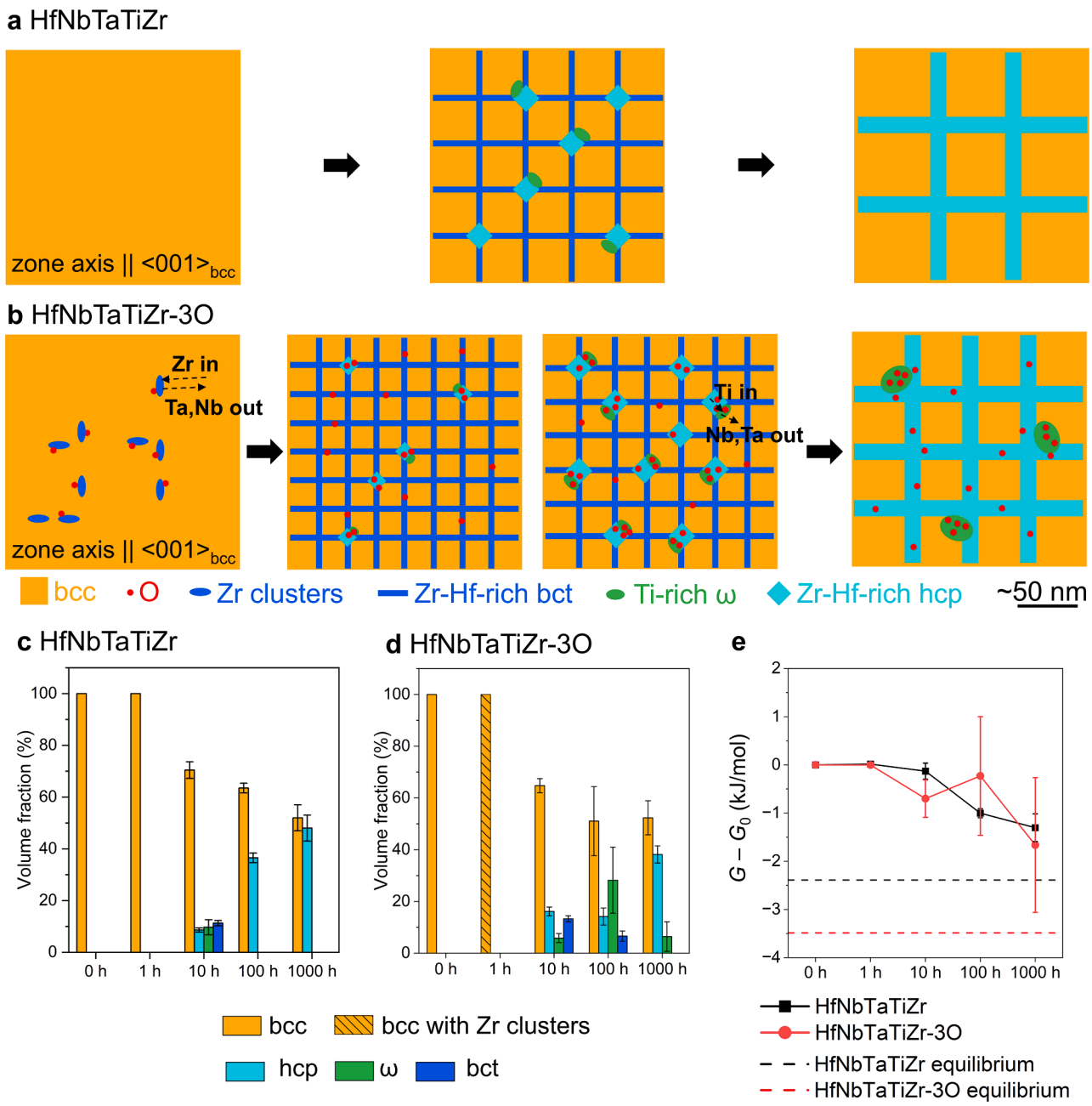

Fig. 10. Schematic drawings illustrating microstructural evolution in (a) HfNbTaTiZr and (b) HfNbTaTiZr-3O during aging at 500 °C. Temporal evolution of volume fractions of different phases in (c) HfNbTaTiZr and (d) HfNbTaTiZr-3O during aging. (e) Temporal evolution of the total molar Gibbs free energy of the system G relative to the as-received state G_0 of HfNbTaTiZr and HfNbTaTiZr-3O during aging; the determination of the error bars is given in Supplementary Material, section G.

from the enhanced elastic instability of bcc phase due to the addition of O. For a cubic system, the modified Born criterion under a hydrostatic pressure P is expressed as $(C_{11}–C_{12}–2P)(C_{11}+2C_{12}+P)$. A positive value means that the lattice is dynamically stable, whereas a negative value suggests instability. When $P = 0$, the expression is reduced to $(C_{11}–C_{12})(C_{11}+2C_{12}) > 0$ for a dynamically stable lattice [68]. The elastic stiffness constants of the bcc HfNbTaTiZr and HfNbTaTiZr-3O under different conditions were calculated using TCTI6 database in Thermo-Calc, as listed in Table S4. We found that the as-received HfNbTaTiZr, HfNbTaTiZr-3O, and the bcc phase with the 10-h bct composition in HfNbTaTiZr fulfill the criterion. In contrast, the bcc phase with 10-h bct composition in HfNbTaTiZr-3O violates it, indicating that O might reduce the lattice stability and thus assisting the formation of the bct phase.

The formation of bct channels along $<001>_{bcc}$ directions could be associated with the elastic anisotropy of the alloy. Indeed, elastic anisotropy is known to influence the crystallographic direction of compositional modulations [69,70]. In this context, the Zener anisotropy ratio $A = 2C_{44}/(C_{11}–C_{12})$ [71] is usually used to quantify the degree of elastic anisotropy of cubic crystals. The calculated Zener anisotropy ratio A for HfNbTaTiZr and HfNbTaTiZr-3O is 3.3 and 4.8, respectively, both larger than 1. In this case, the orientation-dependent Young's modulus is minimum along $<001>_{bcc}$ directions, which allows the elastic strain energy associated with the lattice misfit between channels and cuboids to be minimized [58].

Regarding the lattice distortion of the bcc matrix, the formation of the Zr-Hf-rich bct channels induces a chemical change of the bcc matrix and hence a change in the lattice distortion. The size mismatch in bcc

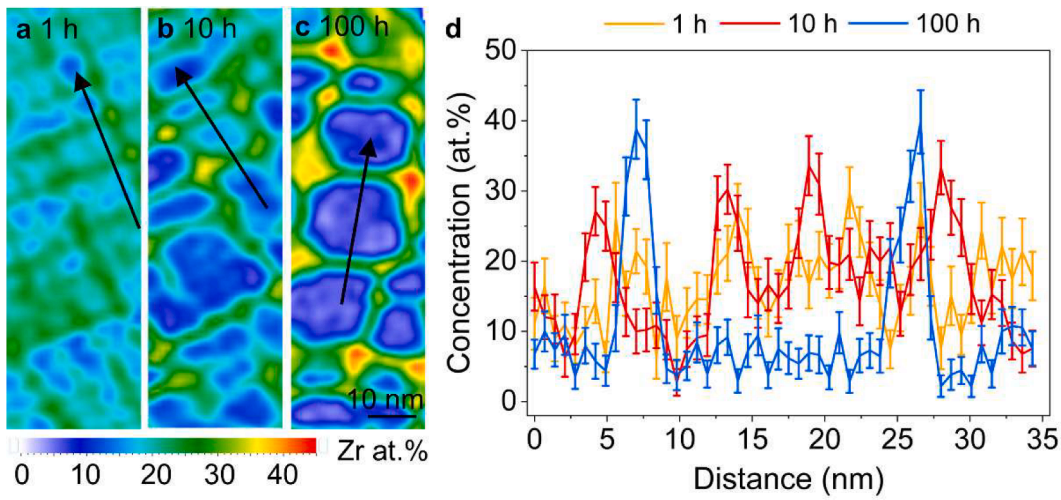

Fig. 11. (a), (b), and (c) 2D concentration maps of Zr in a 5-nm thick ROI in the 1-h aged, 10-h aged, and 100-aged HfNbTaTiZr-3O, respectively. (d) 1D concentration profiles recorded along the 35-nm long arrows in (a-c) showing compositional modulation of Zr across matrix and channels (orange for 1-h, red for 10-h, and blue for 100-h aged samples).

matrix of the HfNbTaTiZr under as-received condition and aged for 10 h was calculated using the bcc composition determined by APT (Table S1) in combination with

$$\delta = \sqrt{\sum_{i=1}^{N} c_i \left(1 - \frac{r_i}{\sum_{i=1}^{N} c_i r_i}\right)^2} \quad (1)$$

to estimate the lattice distortion[2] [72]. It is found that before the formation of bct channels, the size mismatch of bcc single phase is 5.8 %, while the value is reduced to 5.4 % after the formation of bct channels. Therefore, the formation of bct channels along $<001>_{bcc}$ reduces lattice distortion within the bcc matrix. This lattice relaxation was also evidenced by experiments and simulations in the work of Maiti and Steure [17], who show that the tetragonal relaxation is attributed to Zr clustering along $<001>_{bcc}$ directions.

4.3. Impact of oxygen on the stability of bct channels

The TEM and APT characterizations demonstrate that the addition of 3 at.% O to HfNbTaTiZr promotes Zr segregation to form precursors of bct channels after aging for 1 h. Moreover, compared to HfNbTaTiZr, a higher O content in HfNbTaTiZr-3O results in the activation of more nucleation sites for channel formation. Thus, the mean distance between the bct channels in the 10-h aged HfNbTaTiZr-3O is smaller than that in HfNbTaTiZr.

It is noted that the average thickness of the channels after 10 h of aging is smaller in HfNbTaTiZr-3O (~2.1 nm) than in HfNbTaTiZr (~2.7 nm), meaning that the growth rate of a bct channel is slightly slower due to the addition of 3 at.% O. The Zr-Hf-concentration in the bct phase of HfNbTaTiZr-3O is lower, indicating that their segregation to the bct channels is suppressed. These observations likely resulted from several influencing factors: (a) The numbers density of the nucleation sites of bct phase in HfNbTaTiZr-3O is higher than that in HfNbTaTiZr. Since the distance between the nucleation sites is smaller in the former, it is possible that the overlapped diffusion field of the neighboring nuclei the growth rate of the bct phase in HfNbTaTiZr-3O due to soft impingement [73]. (b) Within a constant volume, the higher number density of the Zr (O)-segregation as bct precursors in HfNbTaTiZr-3O provides more diffusion destinations for Zr and Hf than in HfNbTaTiZr. Thus, Zr/Hf are distributed into more dispersed channels in HfNbTaTiZr-3O and dilute their concentrations in the individual channel, slowing down its growth rate. (c) Hcp phase, which is stabilized by Zr and Hf, is also observed in both alloys after 10 h of aging. It has similar sizes in both alloys, but its volume fraction is doubled in HfNbTaTiZr-3O than in HfNbTaTiZr (compare Figs. 10c and 10d). The concentration of Zr-Hf in the bct phase is thus reduced due to the stabilization of hcp phase in the alloy added with O. (d) The addition of O could reduce the elemental diffusivities in HfNbTaTiZr-3O (see Table S9), potentially accelerating the growth of the bct phase, but is likely balanced by the other factors.

A comparison of Figs. 1 and 4 reveals that the addition of O retards the transformation from bct channel to hcp, which is accompanied by an increase in Zr and Hf concentrations, as indicated by the compositional evolution in Figs. 3 and 7. In HfNbTaTiZr, the Zr and Hf contents in bct channels are high (Fig. 3f and Table S1), which is already close to the Zr and Hf concentrations of the hcp phase (Fig. 3*g*). This means that the phase transition from bct to hcp may require small amounts of Zr and Hf, which can partition into the hcp phase by diffusion within 10 to 100 h.

Concerning HfNbTaTiZr-3O aged for 10 h, the Zr and Hf concentrations inside the bct channels are lower than those in HfNbTaTiZr aged under the same conditions (compare Figs. 3f and 7f). From 10 to 100 h, the Zr-Hf-rich hcp particles appear at the channel nodes and the ω phase forms at bcc/hcp interfaces, both of which are stabilized by Zr and Hf diffusion from the matrix. Consequently, the Zr and Hf concentrations in the bct channels in HfNbTaTiZr-3O change only slightly from 10 to 100 h aging. As the phase transformation from bct to hcp may require sufficient concentrations of Zr and Hf, which have not been reached after 100 h of aging, the bct-to-hcp transition is delayed in HfNbTaTiZr-3O.

4.4. Effect of oxygen on ω phase stability

Our results reveal that adding 3 at.% O promotes an increasing number density of ω particles with an increasing size. The evolution of ω phase is found to be associated with changes in the bct and hcp compositions.

Ti-rich clusters in the 1-h aged HfNbTaTiZr-3O (Fig. 7e) are close to the Zr-O-rich channels. These Ti-rich clusters may assist the formation of ω particles by providing the appropriate compositional requirements for their nucleation. From 10 to 100 h, the increased number density of hcp particles at channel nodes provides more nucleation sites for ω phase at hcp/bcc interfaces, hence leading to the further population of the ω phase in HfNbTaTiZr-3O aged from 10 to 100 h.

Regarding the growth of ω particles from 10 to 1000 h, detailed APT

[2] Oxygen concentration is excluded as δ is only valid for substitutional elements.

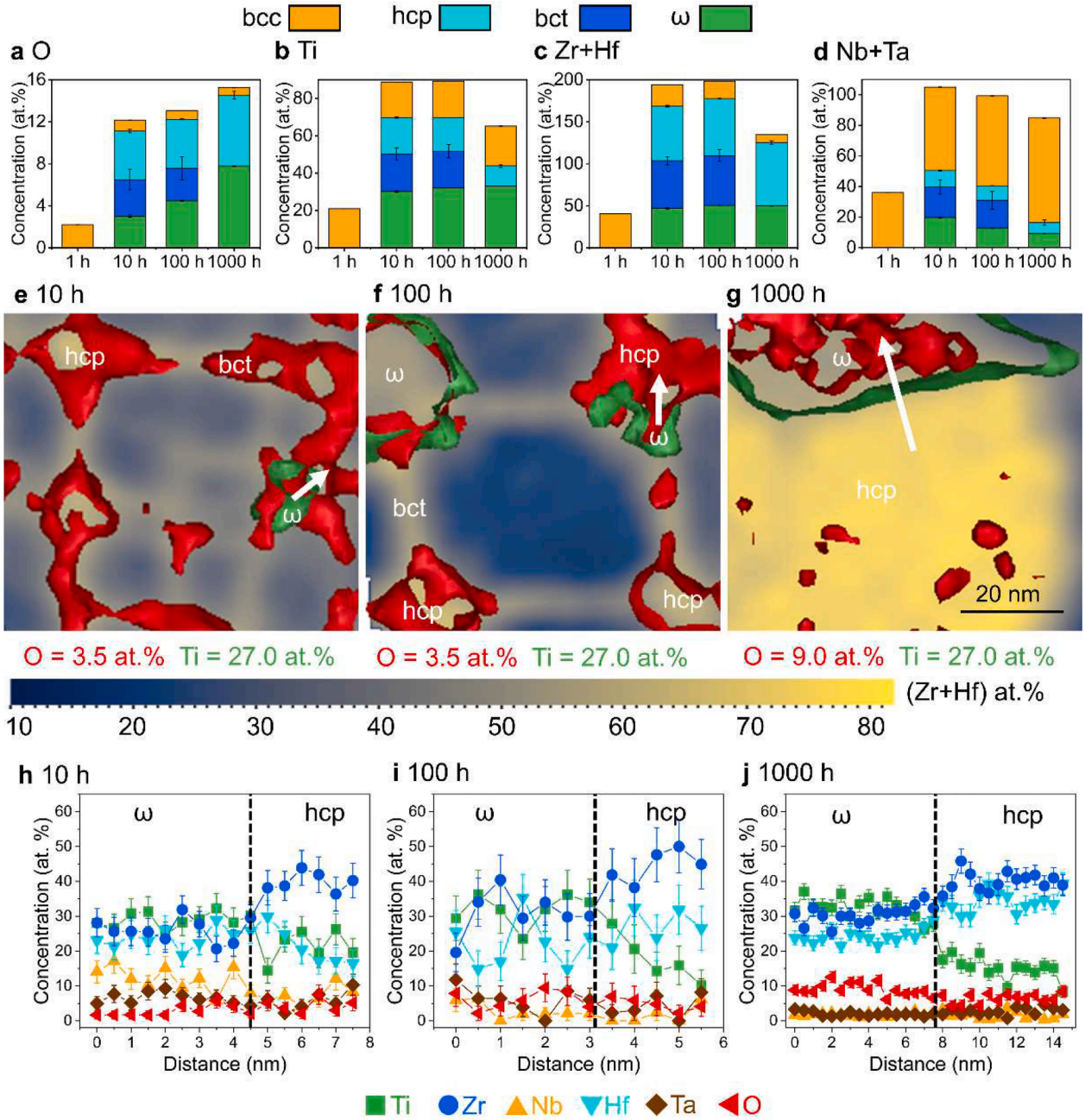

Fig. 12. Temporal concentration evolutions of (a) O, (b) Ti, (c) Zr+Hf, and (d) Nb+Ta in the bcc matrix, bct, hcp, and ω phases in HfNbTaTiZr-3O. 2D concentration maps of Zr+Hf obtained from an ROI with a thickness of 5 nm overlaid with isoconcentration surfaces of O (in red) and Ti (in green) in the alloy aged for (e) 10 h, (f) 100 h, and (g) 1000 h. (h), (i), and (j) 1D concentration profiles across ω/hcp interfaces recorded along the white arrows in (e), (f), and (g), respectively.

analyses were carried out to reveal the elemental partitioning behaviors in the four different phases (Figs. 12a-d). During aging, the O concentration increases in the ω and hcp phases, while it decreases in the bcc matrix and bct channels, Fig. 12a. Thus, O atoms diffuse into ω and hcp from the bcc matrix and bct channels. As shown in Fig. 12e, the O content is locally enriched in all the three secondary phases of the 10-h aged HfNbTaTiZr-3O: channel nodes, ω particles, and the channels, represented by 3.5 at. % O isoconcentration surfaces. Along the arrow in Fig. 12e, 1D concentration profiles from ω to hcp were recorded and are displayed in Fig. 12h. Here, the O concentration during the early stage of ω precipitation is slightly lower in ω than in hcp. As aging time increases to 100 h, O atoms partition mostly to coarse hcp and ω particles, in which the O concentration increases without any obvious preferential partitioning between them, thus confirming that the O-diffusion from bct and bcc stabilizes the ω and hcp phases (Figs. 12f and 12i). As time further increases to 1000 h, although some ω disappears, the O concentration in the remaining ω is even higher than in hcp, indicated by the 9.0 at. % O isoconcentration surface in Fig. 12g and the O concentration profile in Fig. 12j. Our APT results prove the increasingly preferential partitioning of O into ω in HfNbTaTiZr-3O upon aging at 500 °C, which plays a major role in ω phase stabilization.

Another important factor for ω stabilization is Ti segregation. As shown in Fig. 12b, the Ti concentration slightly increases in the ω phase between 10 and 1000 h, while it decreases in the hcp phase. Moreover, the 1D concentration profiles in Figs. 12h-j show that there is a Ti concentration gradient within hcp particles, i.e., Ti concentration is lower at the center of the particles and higher close to the ω/hcp interface (e.g., Fig. 12i), which indicates that Ti atoms are likely rejected

from hcp particles during their growth, inducing a local Ti-enrichment at bcc/hcp interfaces, where ω particles form.

It is also noticed that the Zr and Hf concentrations in the ω phase are both higher than 20 at. %, indicating that this phase is also stabilized by these elements. From 10 to 100 h, the Zr-Hf-rich bct channels partially dissolve, and the remained bct channels almost maintain their Zr+Hf concentration. The content of Zr+Hf in the bcc matrix, however, does not increase but decreases (Fig. 12c). This means the Zr and Hf atoms, originally in the bct channels, diffuse into hcp and ω phases and stabilize them as the aging time increases from 10 to 100 h.

After aging for 1000 h, the hcp phase becomes dominant in the microstructure. The increased Zr and Hf concentrations in hcp between 100 and 1000 h are provided by the complete and partial dissolutions of the bct channels and ω particles, respectively. As a result, the Ti atoms from the ω particles either segregate at phase boundaries displayed in Fig. 7d or redistribute to the bcc matrix forming the Ti-rich clusters shown in Fig. S8.

Along with the evolution of the hcp stabilizers, i.e., O, Ti, Zr, and Hf, the bcc stabilizers Nb and Ta are progressively rejected from the ω phase during the aging of HfNbTaTiZr-3O between 10 and 1000 h, as shown in Figs. 12d, h-j. In contrast, the ω phase disappears quickly between 10 and 100 h in HfNbTaTiZr. Li and Min [74] revealed that the formation of ω phase is energetically favorable in bcc stabilizer-lean regions in a Ti-15Mo alloy, and lower bcc-stabilizer concentrations in ω phase can ease its structural stabilization with the collapse of $\{111\}_{bcc}$ planes. In this work, it is found that the Nb+Ta concentration in the ω phase in HfNbTaTiZr is slightly higher than that in HfNbTaTiZr-3O after 10 h, and this concentration in the bcc matrix increases more significantly from 10 to 100 h in HfNbTaTiZr (Fig. 3f, Fig. 7f, Table S1, and Table S2). Therefore, the growth of the ω phase in HfNbTaTiZr is likely to encounter higher energy barriers than in HfNbTaTiZr-3O, making the ω phase less stable. In addition, the bct channels transform into hcp particles, accompanied by the rejection of Nb and Ta from 10 to 100 h, which leads to an increase in Nb and Ta concentrations in the bcc matrix and inhibits the nucleation of ω phase in HfNbTaTiZr during aging.

4.5. Estimation of critical resolved shear stress (CRSS) and precipitation strengthening

The *CRSS* of the bcc HfNbTaTiZr solid solution can be estimated from the tensile yield stress of the polycrystalline alloy or deduced from micropillar compression of $<001>_{bcc}$-oriented single crystals of the same alloy. Considering the individual strengthening contributions in HfNbTaTiZr, the yield stress can be estimated using:

$$\sigma_{ys} = \sigma_{gb} + \sigma_{ss} + \sigma_{p} + \sigma_{dis} \quad (2)$$

where σ_{gb}, σ_{ss}, σ_{dis}, σ_{p}, and σ_{dis} are grain boundary, solid solution (including friction stress), precipitation, and dislocation strengthening, respectively [67,75,76]. Since there are no secondary phases in the as-received condition and the dislocation density is expected to be low after homogenization annealing, the tensile yield stress of the bcc single-phase HfNbTaTiZr mainly originates from solid solution and grain boundary strengthening. The latter is evaluated using the Hall-Petch equation [77]:

$$\sigma_{gb} = kd^{-1/2} \quad (3)$$

where k is a Hall-Petch coefficient and d denotes the mean grain size. For HfNbTaTiZr, k is ~240 MPa $\mu m^{1/2}$ according to [78]. With an average grain size of ~80 μm [29], the grain boundary strengthening is estimated to be 27 MPa. Using Eq. (2) where σ_p and σ_{dis} are negligible, the *CRSS* can be calculated from:

$$CRSS = \tau_{ss} = \sigma_{ss}/M = (\sigma_{ys} - \sigma_{gb})/M \quad (4)$$

where $M = 3.06$ is the Taylor factor for an isotropic polycrystal [79]. Inserting $\sigma_{ys} = 960$ MPa into Eq. (4) gives a *CRSS* for HfNbTaTiZr of ~305 MPa. This value is lower than the reported *CRSS* = 449 MPa by Yasuda et al. [13], which could be attributed to the tension-compression asymmetrical deformation behavior of bcc metals [80,81].

The *CRSS* can also be estimated from micropillar compression. In the present work, the yield stress of HfNbTaTiZr micropillars with a loading axis parallel to $<001>_{bcc}$ was found to be 670 ± 30 MPa, the *CRSS* is calculated from:

$$CRSS = S\sigma_{ys} \quad (5)$$

where $S = 0.47$ is the Schmid factor [82], which is maximum for the $\{11\bar{2}\}<111>$ system. A *CRSS* value of ~315 MPa is then obtained for HfNbTaTiZr. Similarly, we calculated a *CRSS* of ~405 MPa for the as-received HfNbTaTiZr-3O, indicating that the magnitude of interstitial strengthening by O in HfNbTaTiZr represents ~30 MPa per atomic percent of O for the *CRSS* with a loading direction parallel to $<001>_{bcc}$. As indicated in the previous works [59,83,84], the *CRSS* of HfNbTaTiZr is dependent on the loading direction and strain rate. Furthermore, size effect could also influence the *CRSS* [85,86]. These factors should be carefully investigated in future research.

Upon aging at 500 °C, various secondary phases form in HfNbTaTiZr and HfNbTaTiZr-3O, and their volume fractions evolve with time. The secondary phases interact with dislocations, resulting in precipitation strengthening. Meanwhile, solid solution strengthening of the bcc matrix varies during aging along with its compositional evolution. The change of *CRSS* due to the microstructural evolution of the two alloys are estimated based on cutting, Orowan mechanisms [67] and their modified models for different precipitate morphologies [87], as listed in Table S5 and discussed in the supplementary material section E. It is found that the nanosized phases play a dominant role in the precipitation strengthening of the HfNbTaTiZr and HfNbTaTiZr-3O during aging.

5. Conclusions

Combining TEM and APT techniques allowed us to shed light on the detailed structural and compositional changes in HfNbTaTiZr with and without 3 at.% O addition during aging at 500 °C. The effects of O on the formation and stabilization of metastable/stable phases were addressed and the resulting mechanical properties were comprehensively studied. The following conclusions are drawn from our experiments:

1. After aging at 500 °C for 10 h, ~2.7-nm thick metastable bct channels along $<001>_{bcc}$ directions forming a network are observed in HfNbTaTiZr. Their formation is associated with Zr-Hf-segregation, leading to lattice relaxation of the bcc parent phase. Zr-Hf-rich hcp particles with a size of ~3.6 nm form at channel nodes. In addition, ~11.1-nm Ti-rich metastable ω-phase particles form at bcc/hcp interfaces. With increasing aging time from 100 to 1000 h, the ω phase dissolves and the bct channels gradually transform into a distorted hcp phase with a coarser microstructure.
2. The addition of 3 at.% O to HfNbTaTiZr promotes Zr segregation, which accelerates the formation of more dispersed and thinner bct channels (~2.1-nm thick) upon aging at 500 °C. The induced Ti-modulation at bcc/bct interfaces acts as nucleation sites for ω particles after aging for 1 h. As aging proceeds from 10 to 100 h, the ω phase populates and grows. The partial dissolution of the bct channels and Ti rejection from the hcp phase at channel nodes are thought to assist ω-phase formation. As a result, the bct-channel composition does not change significantly with time and the bct-to-hcp transformation is hence delayed from 100 to 1000 h.
3. Mechanical tests on the alloys revealed that the formation of metastable phases provides a hardening effect at the expense of ductility. Although O induces an embrittlement mainly at grain boundaries, it promotes the formation of a finer nanoscale microstructure within the grains, which strongly improves the strength.

Disclosure statement

The authors declare no potential conflict of interest related to this work.

CRediT authorship contribution statement

Yujun Zhao: Writing – review & editing, Writing – original draft, Visualization, Validation, Investigation, Formal analysis, Data curation. **Maik Rajkowski:** Validation, Investigation. **Yilun Gong:** Investigation, Resources, Validation, Writing – review & editing. **Stephan Laube:** Resources. **Loïc Perrière:** Resources. **Alexander Kauffmann:** Writing – review & editing, Resources. **Jean-Philippe Couzinié:** Writing – review & editing, Resources. **Guillaume Laplanche:** Writing – review & editing, Supervision, Resources, Funding acquisition. **Tong Li:** Writing – review & editing, Supervision, Resources, Project administration, Funding acquisition, Conceptualization.

Declaration of competing interest

The authors declare that they have no known competing financial interests or personal relationships that could have appeared to influence the work reported in this paper.

Acknowledgment

The authors would like to thank Deutsche Forschungsgemeinschaft (DFG)/SPP 2006 for financial support through projects TL 3272/6–2 and LA 3607/3–2 (common project number 388735491), Zentrum für Grenzflächendominierte Höchstleistungswerkstoffe (ZGH) at Ruhr University Bochum for the access of infrastructures.

Supplementary materials

Supplementary material associated with this article can be found, in the online version, at doi:10.1016/j.actamat.2025.121400.

Reference

[1] O.N. Senkov, D.B. Miracle, K.J. Chaput, J.-P. Couzinie, Development and exploration of refractory high entropy alloys—A review, J. Mater. Res. 33 (2018) 3092–3128, https://doi.org/10.1557/jmr.2018.153.

[2] S. Dixit, S. Rodriguez, M.R. Jones, P. Buzby, R. Dixit, N. Argibay, F.W. DelRio, H. H. Lim, D. Fleming, Refractory High-Entropy Alloy Coatings for High-Temperature Aerospace and Energy Applications, J. Therm. Spray Technol. 31 (2022) 1021–1031, https://doi.org/10.1007/s11666-022-01324-0.

[3] M. Moschetti, A. Hohenwarter, M. Alfreider, J. Couzinié, T. Wei, J. Davis, A. Xu, D. Bhattacharyya, J.J. Kruzic, B. Gludovatz, Fracture Toughness Investigations of an Ion-Irradiated Nanocrystalline TiZrNbHfTa Refractory High-Entropy Alloy, Adv. Eng. Mater. (2024) 2400541, https://doi.org/10.1002/adem.202400541.

[4] E.J. Pickering, A.W. Carruthers, P.J. Barron, S.C. Middleburgh, D.E.J. Armstrong, A.S. Gandy, High-Entropy Alloys for Advanced Nuclear Applications, Entropy 23 (2021) 98, https://doi.org/10.3390/e23010098.

[5] W. Jia, Y. Gong, K. Zheng, Y. Ma, X. Zheng, Y. Wu, B. Zhou, J. Gao, S. Yu, Mechanical properties and biological behavior of refractory TiZrNbTa medium-entropy and TiZrHfNbTa high-entropy alloy nanofilms on AISI 316l for bone implants, Mater. Charact. 216 (2024) 114253, https://doi.org/10.1016/j.matchar.2024.114253.

[6] A. Motallebzadeh, N.S. Peighambardoust, S. Sheikh, H. Murakami, S. Guo, D. Canadinc, Microstructural, mechanical and electrochemical characterization of TiZrTaHfNb and Ti1.5ZrTa0.5Hf0.5Nb0.5 refractory high-entropy alloys for biomedical applications, Intermetallics 113 (2019) 106572, https://doi.org/10.1016/j.intermet.2019.106572.

[7] O.N. Senkov, J.M. Scott, S.V. Senkova, D.B. Miracle, C.F. Woodward, Microstructure and room temperature properties of a high-entropy TaNbHfZrTi alloy, J. Alloys Compd. 509 (2011) 6043–6048, https://doi.org/10.1016/j.jallcom.2011.02.171.

[8] L.H. Mills, M.G. Emigh, C.H. Frey, N.R. Philips, S.P. Murray, J. Shin, D.S. Gianola, T.M. Pollock, Temperature-dependent tensile behavior of the HfNbTaTiZr multi-principal element alloy, Acta Mater 245 (2023) 118618, https://doi.org/10.1016/j.actamat.2022.118618.

[9] O.N. Senkov, A.L. Pilchak, S.L. Semiatin, Effect of Cold Deformation and Annealing on the Microstructure and Tensile Properties of a HfNbTaTiZr Refractory High Entropy Alloy, Metall. Mater. Trans. A 49 (2018) 2876–2892, https://doi.org/10.1007/s11661-018-4646-8.

[10] B. Schuh, B. Völker, J. Todt, N. Schell, L. Perrière, J. Li, J.P. Couzinié, A. Hohenwarter, Thermodynamic instability of a nanocrystalline, single-phase TiZrNbHfTa alloy and its impact on the mechanical properties, Acta Mater 142 (2018) 201–212, https://doi.org/10.1016/j.actamat.2017.09.035.

[11] S.Y. Chen, Y. Tong, K.-K. Tseng, J.-W. Yeh, J.D. Poplawsky, J.G. Wen, M.C. Gao, G. Kim, W. Chen, Y. Ren, R. Feng, W.D. Li, P.K. Liaw, Phase transformations of HfNbTaTiZr high-entropy alloy at intermediate temperatures, Scr. Mater. 158 (2019) 50–56, https://doi.org/10.1016/j.scriptamat.2018.08.032.

[12] N.D. Stepanov, N.Yu. Yurchenko, S.V. Zherebtsov, M.A. Tikhonovsky, G. A. Salishchev, Aging behavior of the HfNbTaTiZr high entropy alloy, Mater. Lett. 211 (2018) 87–90, https://doi.org/10.1016/j.matlet.2017.09.094.

[13] H.Y. Yasuda, Y. Yamada, K. Cho, T. Nagase, Deformation behavior of HfNbTaTiZr high entropy alloy singe crystals and polycrystals, Mater. Sci. Eng. A 809 (2021) 140983, https://doi.org/10.1016/j.msea.2021.140983.

[14] M. Moschetti, A. Xu, A. Hohenwarter, T. Wei, J. Davis, K. Short, G.J. Thorogood, C. Kong, J.-P. Couzinié, D. Bhattacharyya, J.J. Kruzic, B. Gludovatz, The Influence of Phase Formation on Irradiation Tolerance in a Nanocrystalline TiZrNbHfTa Refractory High-Entropy Alloy, Adv. Eng. Mater. 26 (2024) 2300863, https://doi.org/10.1002/adem.202300863.

[15] S. Wang, M. Wu, D. Shu, G. Zhu, D. Wang, B. Sun, Mechanical instability and tensile properties of TiZrHfNbTa high entropy alloy at cryogenic temperatures, Acta Mater 201 (2020) 517–527, https://doi.org/10.1016/j.actamat.2020.10.044.

[16] C. Wu, L.S. Aota, J. Rao, X. Zhang, L. Perrière, M.J. Duarte, D. Raabe, Y. Ma, Hydrogen-assisted spinodal decomposition in a TiNbZrHfTa complex concentrated alloy, Acta Mater 285 (2025) 120707, https://doi.org/10.1016/j.actamat.2024.120707.

[17] S. Maiti, W. Steurer, Phase stability, local chemical disorder and its effect on the mechanical properties of refractory high-entropy alloys, (2016). https://doi.org/10.48550/ARXIV.1601.06015.

[18] Z. Lei, Y. Wu, J. He, X. Liu, H. Wang, S. Jiang, L. Gu, Q. Zhang, B. Gault, D. Raabe, Z. Lu, Snoek-type damping performance in strong and ductile high-entropy alloys, Sci. Adv. 6 (2020) eaba7802, https://doi.org/10.1126/sciadv.aba7802.

[19] Z. Lei, X. Liu, Y. Wu, H. Wang, S. Jiang, S. Wang, X. Hui, Y. Wu, B. Gault, P. Kontis, D. Raabe, L. Gu, Q. Zhang, H. Chen, H. Wang, J. Liu, K. An, Q. Zeng, T.-G. Nieh, Z. Lu, Enhanced strength and ductility in a high-entropy alloy via ordered oxygen complexes, Nature 563 (2018) 546–550, https://doi.org/10.1038/s41586-018-0685-y.

[20] C.H. Belcher, B.E. MacDonald, D. Apelian, E.J. Lavernia, The role of interstitial constituents in refractory complex concentrated alloys, Prog. Mater. Sci. 137 (2023) 101140, https://doi.org/10.1016/j.pmatsci.2023.101140.

[21] E. Osei-Agyemang, G. Balasubramanian, Surface oxidation mechanism of a refractory high-entropy alloy, Npj Mater. Degrad. 3 (2019) 20, https://doi.org/10.1038/s41529-019-0082-5.

[22] R.J. Lauf, C.J. Altstetter, Diffusion and trapping of oxygen in refractory metal alloys, Acta Metall 27 (1979) 1157–1163, https://doi.org/10.1016/0001-6160(79)90133-0.

[23] Z. Liu, G. Welsch, Literature Survey on Diffusivities of Oxygen, Aluminum, and Vanadium in Alpha Titanium, Beta Titanium, and in Rutile, Metall. Trans. A 19 (1988) 1121–1125, https://doi.org/10.1007/BF02628396.

[24] T. Leveau, L. Ventelon, E. Clouet, Interaction of C, N and O interstitial solute atoms with screw dislocations in HfNbTaTiZr high entropy alloy, Acta Mater 275 (2024) 120062, https://doi.org/10.1016/j.actamat.2024.120062.

[25] R. Poulain, M. Rajkowski, Y. Zhao, P. Gemagami, B. Appolaire, S. Laube, A. Kauffmann, L. Perrière, J.-P. Couzinié, T. Li, G. Laplanche, Oxygen-induced decomposition of the body-centered cubic HfNbTaTiZr high-entropy alloy, Acta Mater (2024) 120295, https://doi.org/10.1016/j.actamat.2024.120295.

[26] J.G. Niu, D.H. Ping, T. Ohno, W.T. Geng, Suppression effect of oxygen on the β to ω transformation in a β -type Ti alloy: insights from first-principles, Model. Simul. Mater. Sci. Eng. 22 (2014) 015007, https://doi.org/10.1088/0965-0393/22/1/015007.

[27] M. Niinomi, M. Nakai, M. Hendrickson, P. Nandwana, T. Alam, D. Choudhuri, R. Banerjee, Influence of oxygen on omega phase stability in the Ti-29Nb-13Ta-4.6Zr alloy, Scr. Mater. 123 (2016) 144–148, https://doi.org/10.1016/j.scriptamat.2016.06.027.

[28] K. Chou, E.A. Marquis, Oxygen effects on ω and α phase transformations in a metastable β Ti–Nb alloy, Acta Mater 181 (2019) 367–376, https://doi.org/10.1016/j.actamat.2019.09.049.

[29] G. Laplanche, P. Gadaud, L. Perrière, I. Guillot, J.P. Couzinié, Temperature dependence of elastic moduli in a refractory HfNbTaTiZr high-entropy alloy, J. Alloys Compd. 799 (2019) 538–545, https://doi.org/10.1016/j.jallcom.2019.05.322.

[30] R. Poulain, M. Rajkowski, Y. Zhao, P. Gemagami, B. Appolaire, S. Laube, A. Kauffmann, L. Perrière, J.-P. Couzinié, T. Li, G. Laplanche, Oxygen-induced decomposition of the body-centered cubic HfNbTaTiZr high-entropy alloy, Acta Mater 280 (2024) 120295, https://doi.org/10.1016/j.actamat.2024.120295.

[31] J. Li, T. Malis, S. Dionne, Recent advances in FIB–TEM specimen preparation techniques, Mater. Charact. 57 (2006) 64–70, https://doi.org/10.1016/j.matchar.2005.12.007.

[32] T.J. Prosa, D.J. Larson, Modern Focused-Ion-Beam-Based Site-Specific Specimen Preparation for Atom Probe Tomography, Microsc. Microanal. 23 (2017) 194–209, https://doi.org/10.1017/S1431927616012642.

[33] B. Gault, A. Saksena, X. Sauvage, P. Bagot, L.S. Aota, J. Arlt, L.T. Belkacemi, T. Boll, Y.-S. Chen, L. Daly, M.B. Djukic, J.O. Douglas, M.J. Duarte, P.J. Felfer, R.G. Forbes, J. Fu, H.M. Gardner, R. Gemma, S.S.A. Gerstl, Y. Gong, G. Hachet, S. Jakob, B.

M. Jenkins, M.E. Jones, H. Khanchandani, P. Kontis, M. Krämer, M. Kühbach, R.K. W. Marceau, D. Mayweg, K.L. Moore, V. Nallathambi, B.C. Ott, J.D. Poplawsky, T. Prosa, A. Pundt, M. Saha, T.M. Schwarz, Y. Shang, X. Shen, M. Vrellou, Y. Yu, Y. Zhao, H. Zhao, B. Zou, Towards Establishing Best Practice in the Analysis of Hydrogen and Deuterium by Atom Probe Tomography, Microsc. Microanal. (2024), https://doi.org/10.1093/mam/ozae081.

[34] Y. Chang, A.J. Breen, Z. Tarzimoghadam, P. Kürnsteiner, H. Gardner, A. Ackerman, A. Radecka, P.A.J. Bagot, W. Lu, T. Li, E.A. Jägle, M. Herbig, L.T. Stephenson, M. P. Moody, D. Rugg, D. Dye, D. Ponge, D. Raabe, B. Gault, Characterizing solute hydrogen and hydrides in pure and alloyed titanium at the atomic scale, Acta Mater 150 (2018) 273–280, https://doi.org/10.1016/j.actamat.2018.02.064.

[35] F. Vurpillot, J. Houard, A. Vella, B. Deconihout, Thermal response of a field emitter subjected to ultra-fast laser illumination, J. Phys. Appl. Phys. 42 (2009) 125502, https://doi.org/10.1088/0022-3727/42/12/125502.

[36] G. Nolze, R. Hielscher, Orientations – perfectly colored, J. Appl. Crystallogr. 49 (2016) 1786–1802, https://doi.org/10.1107/S1600576716012942.

[37] S.K. Sikka, Y.K. Vohra, R. Chidambaram, Omega phase in materials, Prog. Mater. Sci. 27 (1982) 245–310, https://doi.org/10.1016/0079-6425(82)90002-0.

[38] W.G. Burgers, On the process of transition of the cubic-body-centered modification into the hexagonal-close-packed modification of zirconium, Physica 1 (1934) 561–586, https://doi.org/10.1016/S0031-8914(34)80244-3.

[39] Y. Shen, Y. Jiang, J. Lin, C. Wang, J. Sun, Can single crystal X-ray diffraction determine a structure uniquely?, (2020). https://doi.org/10.48550/ARXIV.2008.10008.

[40] U. Müller, Symmetry Relationships between Crystal Structures: Applications of Crystallographic Group Theory in Crystal Chemistry, Oxford University Press, 2013, https://doi.org/10.1093/acprof:oso/9780199669950.001.0001.

[41] S.G. Srinivasan, D.M. Hatch, H.T. Stokes, A. Saxena, R.C. Albers, T. Lookman, Mechanism for BCC to HCP Transformation: generalization of the Burgers Model, (2002). https://doi.org/10.48550/ARXIV.COND-MAT/0209530.

[42] L.A. Bendersky, A. Roytburd, W.J. Boettinger, Phase transformations in the (Ti, Al) 3 Nb section of the Ti Al Nb system—I. Microstructural predictions based on a subgroup relation between phases, Acta Metall. Mater. 42 (1994) 2323–2335, https://doi.org/10.1016/0956-7151(94)90311-5.

[43] J.-Y. Yan, G.B. Olson, Molar volumes of bcc, hcp, and orthorhombic Ti-base solid solutions at room temperature, Calphad 52 (2016) 152–158, https://doi.org/10.1016/j.calphad.2016.01.003.

[44] J.W. Cahn, W. Rosenberg, On the tetragonality of substitutional martensites, Scr. Metall. 5 (1971) 101–103, https://doi.org/10.1016/0036-9748(71)90038-X.

[45] H.P. Ng, P. Nandwana, A. Devaraj, M. Semblanet, S. Nag, P.N.H. Nakashima, S. Meher, C.J. Bettles, M.A. Gibson, H.L. Fraser, B.C. Muddle, R. Banerjee, Conjugated precipitation of twin-related α and Ti2Cu phases in a Ti–25V–3Cu alloy, Acta Mater 84 (2015) 457–471, https://doi.org/10.1016/j.actamat.2014.10.053.

[46] S. Banerjee, P. Mukhopadhyay, Phase Transformations: Examples from Titanium and Zirconium Alloys, Elsevier Science, 2010. https://books.google.de/books?id=46ECHriRKkUC.

[47] J. Reitz, C. Lochbichler, B. Friedrich, Recycling of gamma titanium aluminide scrap from investment casting operations, Intermetallics 19 (2011) 762–768, https://doi.org/10.1016/j.intermet.2010.11.015.

[48] T. Zhang, X. Meng, C. Wang, L. Li, J. Yang, W. Li, R. Li, Y. Zhang, Investigations of new bulk metallic glass alloys fabricated using a high-pressure die-casting method based on industrial grade Zr raw material, J. Alloys Compd. 792 (2019) 851–859, https://doi.org/10.1016/j.jallcom.2019.03.357.

[49] M.P. Moody, L.T. Stephenson, P.V. Liddicoat, S.P. Ringer, Contingency table techniques for three dimensional atom probe tomography, Microsc. Res. Tech. 70 (2007) 258–268, https://doi.org/10.1002/jemt.20412.

[50] M.P. Moody, L.T. Stephenson, A.V. Ceguerra, S.P. Ringer, Quantitative binomial distribution analyses of nanoscale like-solute atom clustering and segregation in atom probe tomography data, Microsc. Res. Tech. 71 (2008) 542–550, https://doi.org/10.1002/jemt.20582.

[51] Y.-C. Huang, Y.-C. Lai, Y.-H. Lin, S.-K. Wu, A study on the severely cold-rolled and annealed quaternary equiatomic derivatives from quinary HfNbTaTiZr refractory high entropy alloy, J. Alloys Compd. 855 (2021) 157404, https://doi.org/10.1016/j.jallcom.2020.157404.

[52] H. Dobbelstein, E.P. George, E.L. Gurevich, A. Kostka, A. Ostendorf, G. Laplanche, Laser metal deposition of refractory high-entropy alloys for high-throughput synthesis and structure-property characterization, Int. J. Extreme Manuf. 3 (2021) 015201, https://doi.org/10.1088/2631-7990/abcca8.

[53] H. Khanchandani, B. Gault, Atomic scale understanding of the role of hydrogen and oxygen segregation in the embrittlement of grain boundaries in a twinning induced plasticity steel, Scr. Mater. 234 (2023) 115593, https://doi.org/10.1016/j.scriptamat.2023.115593.

[54] J. Chen, A.M. Dongare, Role of grain boundary character on oxygen and hydrogen segregation-induced embrittlement in polycrystalline Ni, J. Mater. Sci. 52 (2017) 30–45, https://doi.org/10.1007/s10853-016-0389-3.

[55] P. Lejček, S. Hofmann, Thermodynamics and structural aspects of grain boundary segregation, Crit. Rev. Solid State Mater. Sci. 20 (1995) 1–85, https://doi.org/10.1080/10408439508243544.

[56] J. Wang, Y. Zhao, W. Zhou, Q. Zhao, S. Huang, W. Zeng, In-situ investigation on tensile deformation and fracture behaviors of a new metastable β titanium alloy, Mater. Sci. Eng. A 799 (2021) 140187, https://doi.org/10.1016/j.msea.2020.140187.

[57] J.W. Foltz, B. Welk, P.C. Collins, H.L. Fraser, J.C. Williams, Formation of Grain Boundary α in β Ti Alloys: its Role in Deformation and Fracture Behavior of These Alloys, Metall. Mater. Trans. A 42 (2011) 645–650, https://doi.org/10.1007/s11661-010-0322-3.

[58] D.A. Porter, K.E. Easterling, K.E. Easterling, Phase Transformations in Metals and Alloys (Revised Reprint), 0 ed., CRC Press, 2009 https://doi.org/10.1201/9781439883570.

[59] T. Tsuru, S. Han, S. Matsuura, Z. Chen, K. Kishida, I. Iobzenko, S.I. Rao, C. Woodward, E.P. George, H. Inui, Intrinsic factors responsible for brittle versus ductile nature of refractory high-entropy alloys, Nat. Commun. 15 (2024) 1706, https://doi.org/10.1038/s41467-024-45639-8.

[60] V.P. Skripov, A.V. Skripov, Spinodal decomposition (phase transitions via unstable states), Sov. Phys. Uspekhi 22 (1979) 389–410, https://doi.org/10.1070/PU1979v022n06ABEH005571.

[61] J.W. Cahn, On spinodal decomposition, Acta Metall 9 (1961) 795–801, https://doi.org/10.1016/0001-6160(61)90182-1.

[62] P. Paufler, B.K. Vainshtein, V.M. Fridkin, V.L. Indenbom, Structure of Crystals. Modern Crystallography, Vol. 2. Springer-Verlag Berlin. 2nd, enlarged Edition 1995. 423 Abb., XX + 520 Seiten. Leinen DM 119, — ISBN 3–540–56848–4, Cryst, Res. Technol. 30 (1995) 948, https://doi.org/10.1002/crat.2170300713. –948.

[63] E. Clementi, D.L. Raimondi, Atomic Screening Constants from SCF Functions, J. Chem. Phys. 38 (1963) 2686–2689, https://doi.org/10.1063/1.1733573.

[64] S. Mishra, S. Maiti, B.S. Dwadasi, B. Rai, Realistic microstructure evolution of complex Ta-Nb-Hf-Zr high-entropy alloys by simulation techniques, Sci. Rep. 9 (2019) 16337, https://doi.org/10.1038/s41598-019-52170-0.

[65] M.M.J. Treacy, J.M. Gibson, The effects of elastic relaxation on transmission electron microscopy studies of thinned composition-modulated materials, J. Vac. Sci. Technol. B Microelectron. Process. Phenom. 4 (1986) 1458–1466, https://doi.org/10.1116/1.583473.

[66] H.Y. Yasuda, Y. Yamada, M. Onishi, H. Suzuki, K. Cho, S. Ichikawa, T. Nagase, Stress increase by nanoscale hcp precipitates in HfNbTaTiZr high entropy alloys, Scr. Mater. 255 (2025) 116401, https://doi.org/10.1016/j.scriptamat.2024.116401.

[67] G. Gottstein, Physical Foundations of Materials Science, Springer Berlin Heidelberg, Berlin, Heidelberg, 2004, https://doi.org/10.1007/978-3-662-09291-0.

[68] G. Grimvall, B. Magyari-Köpe, V. Ozoliņš, K.A. Persson, Lattice instabilities in metallic elements, Rev. Mod. Phys. 84 (2012) 945–986, https://doi.org/10.1103/RevModPhys.84.945.

[69] J.W. Cahn, On spinodal decomposition in cubic crystals, Acta Metall 10 (1962) 179–183, https://doi.org/10.1016/0001-6160(62)90114-1.

[70] T.A. Abinandanan, F. Haider, An extended Cahn-Hilliard model for interfaces with cubic anisotropy, MRS Proc 696 (2001) T7.4, https://doi.org/10.1557/PROC-696-T7.4.

[71] C. Zener, Contributions to the Theory of Beta-Phase Alloys, Phys. Rev. 71 (1947) 846–851, https://doi.org/10.1103/PhysRev.71.846.

[72] Y. Zhang, Y.J. Zhou, J.P. Lin, G.L. Chen, P.K. Liaw, Solid-Solution Phase Formation Rules for Multi-component Alloys, Adv. Eng. Mater. 10 (2008) 534–538, https://doi.org/10.1002/adem.200700240.

[73] P. Franke, G. Inden, Diffusion controlled transformations in multi-particle systems, Int. J. Mater. Res. 88 (2021) 917–924.

[74] M. Li, X. Min, Origin of ω-phase formation in metastable β-type Ti-Mo alloys: cluster structure and stacking fault, Sci. Rep. 10 (2020) 8664, https://doi.org/10.1038/s41598-020-65254-z.

[75] N. Ali, L. Zhang, D. Liu, H. Zhou, K. Sanaullah, C. Zhang, J. Chu, Y. Nian, J. Cheng, Strengthening mechanisms in high entropy alloys: a review, Mater. Today Commun. 33 (2022) 104686, https://doi.org/10.1016/j.mtcomm.2022.104686.

[76] S. Malopheyev, V. Kulitskiy, R. Kaibyshev, Deformation structures and strengthening mechanisms in an Al Mg *Sc* Zr alloy, J. Alloys Compd. 698 (2017) 957–966, https://doi.org/10.1016/j.jallcom.2016.12.289.

[77] E.O. Hall, The Deformation and Ageing of Mild Steel: III Discussion of Results, Proc. Phys. Soc. Sect. B 64 (1951) 747–753, https://doi.org/10.1088/0370-1301/64/9/303.

[78] C.-C. Juan, M.-H. Tsai, C.-W. Tsai, W.-L. Hsu, C.-M. Lin, S.-K. Chen, S.-J. Lin, J.-W. Yeh, Simultaneously increasing the strength and ductility of a refractory high-entropy alloy via grain refining, Mater. Lett. 184 (2016) 200–203, https://doi.org/10.1016/j.matlet.2016.08.060.

[79] G.I. Taylor, U. Dehlinger, Strains in Crystalline Aggregate, in: R. Grammel (Ed.), Deform. Flow Solids Verformung Fliessen Festkörp, Springer Berlin Heidelberg, Berlin, Heidelberg, 1956, pp. 3–12, https://doi.org/10.1007/978-3-642-48236-6_2.

[80] G. Taylor, Thermally-activated deformation of BCC metals and alloys, Prog. Mater. Sci. 36 (1992) 29–61, https://doi.org/10.1016/0079-6425(92)90004-Q.

[81] J.W. Christian, Some surprising features of the plastic deformation of body-centered cubic metals and alloys, Metall. Trans. A 14 (1983) 1237–1256, https://doi.org/10.1007/BF02664806.

[82] E. Schmid, W. Boas, Plasticity of crystals, (1950).

[83] M. Sadeghilaridjani, M. Pole, S. Jha, S. Muskeri, N. Ghodki, S. Mukherjee, Deformation and tribological behavior of ductile refractory high-entropy alloys, Wear 478–479 (2021) 203916, https://doi.org/10.1016/j.wear.2021.203916.

[84] M. Tanaka, S. Yamasaki, T. Morikawa, Temperature dependence of the yield stress in TiZrNbHfTa body-centred cubic high-entropy alloy, Mater. Sci. Eng. A 871 (2023) 144917, https://doi.org/10.1016/j.msea.2023.144917.

[85] J.R. Greer, J.Th.M.De Hosson, Plasticity in small-sized metallic systems: intrinsic versus extrinsic size effect, Prog. Mater. Sci. 56 (2011) 654–724, https://doi.org/10.1016/j.pmatsci.2011.01.005.
[86] S. Shahbeyk, G.Z. Voyiadjis, V. Habibi, S.H. Astaneh, M. Yaghoobi, Review of Size Effects during Micropillar Compression Test: experiments and Atomistic Simulations, Crystals 9 (2019) 591, https://doi.org/10.3390/cryst9110591.
[87] J.Liu, B.-S. Li, H. Gardner, Y. Gong, F. Liu, G. He, M. Moorehead, C. Parkin, A. Couet, A.J. Wilkinson, D.E.J. Armstrong, Origin of age softening in the refractory high-entropy alloys, Sci. Adv. 9 (2023) eadj1511, doi:10.1126/sciadv.adj1511.